Resource

TRANSPARENT PROCESS OPEN ACCESS

THE EMBO JOURNAL

Mapping the origin and fate of myeloid cells in distinct compartments of the eye by single-cell profiling

Peter Wieghofer[1,2,*], Nora Hagemeyer[1], Roman Sankowski[1,3], Anja Schlecht[4], Ori Staszewski[1,3], Lukas Amann[1,5], Markus Gruber[4], Jana Koch[1,4], Annika Hausmann[1], Peipei Zhang[4], Stefaniya Boneva[4], Takahiro Masuda[1], Ingo Hilgendorf[6], Tobias Goldmann[1], Chotima Böttcher[7], Josef Priller[7,8,9], Fabio MV Rossi[10], Clemens Lange[4,**,†] & Marco Prinz[1,11,12,***,†]

Abstract

Similar to the brain, the eye is considered an immune-privileged organ where tissue-resident macrophages provide the major immune cell constituents. However, little is known about spatially restricted macrophage subsets within different eye compartments with regard to their origin, function, and fate during health and disease. Here, we combined single-cell analysis, fate mapping, parabiosis, and computational modeling to comprehensively examine myeloid subsets in distinct parts of the eye during homeostasis. This approach allowed us to identify myeloid subsets displaying diverse transcriptional states. During choroidal neovascularization, a typical hallmark of neovascular age-related macular degeneration (AMD), we recognized disease-specific macrophage subpopulations with distinct molecular signatures. Our results highlight the heterogeneity of myeloid subsets and their dynamics in the eye that provide new insights into the innate immune system in this organ which may offer new therapeutic targets for ophthalmological diseases.

Keywords cornea; macrophages; microglia; retina; single-cell RNA-seq
Subject Categories Immunology; Neuroscience
DOI 10.15252/embj.2020105123 | Received 27 March 2020 | Revised 7 December 2020 | Accepted 18 December 2020 | Published online 8 February 2021
The EMBO Journal (2021) 40: e105123

Introduction

Nature has found a way to provide vitally important tissues of the body with immune protection against invading pathogens in a way that greatly reduces the inflammatory response. Beside the brain, certain compartments of the eye such as cornea, lens, retinal pigment epithelium and neural retina, as well as the placenta, ovaries, and testis belong to these tissues. This important feature, known as "immune privilege", is based on several molecular, microanatomical, and cellular factors that constitute and maintain immune protection in a given tissue (Bechmann, 2005).

Several compartments of the eye reside behind specialized blood–tissue barriers that are formed by tight junctions between endothelial cells and other structural specializations, such as tight junctions among ocular pigment epithelial cells (Streilein, 2003). However, these blood–ocular barriers are quite diverse in their location, anatomy, local immune-skewing properties, and the immune cells involved (Shechter *et al*, 2013). For example, the inner blood–retinal barrier, localized within the inner layers of the neural retina, is formed by non-fenestrated endothelial cells, connected by tight junctions and covered by pericytes and astrocyte end feet. In contrast, the blood–aqueous barrier that can be found at the ciliary body consists of fenestrated endothelial cells on the one side, whereas tight junctions connect non-pigmented ciliary epithelium on the side proximal to the aqueous humor (Kaur *et al*, 2008).

1 Institute of Neuropathology, Medical Faculty, University of Freiburg, Freiburg, Germany
2 Institute of Anatomy, Leipzig University, Leipzig, Germany
3 Berta-Ottenstein-Programme for Clinician Scientists, Medical Faculty, University of Freiburg, Freiburg, Germany
4 Eye Center, Medical Center, Medical Faculty, University of Freiburg, Freiburg, Germany
5 Faculty of Biology, University of Freiburg, Freiburg, Germany
6 Department of Cardiology and Angiology I, Medical Faculty, University Heart Center Freiburg, University of Freiburg, Freiburg, Germany
7 Department of Neuropsychiatry and Laboratory of Molecular Psychiatry, Charité—Universitätsmedizin Berlin, Berlin, Germany
8 DZNE and BIH, Berlin, Germany
9 University of Edinburgh and UK DRI, Edinburgh, UK
10 Biomedical Research Centre, University of British Columbia & Faculty of Medicine, University of British Columbia, Vancouver, BC, Canada
11 Signalling Research Centres BIOSS and CIBSS, University of Freiburg, Freiburg, Germany
12 Center for Basics in NeuroModulation (NeuroModulBasics), Medical Faculty, University of Freiburg, Freiburg, Germany
*Corresponding author. Tel: +49 341 97 22053; E-mail: peter.wieghofer@medizin.uni-leipzig.de
**Corresponding author. Tel: +49 761 270 40511; E-mail: clemens.lange@uniklinik-freiburg.de
***Corresponding author. Tel: +49 761 270 51060; E-mail: marco.prinz@uniklinik-freiburg.de
†These authors contributed equally to this work

Finally, the cornea and the anterior chamber are specialized immune-privileged sites of the eye that are transparent and avascular while other compartments lack blood–tissue barriers such as the choroid or conjunctiva. Despite their different localizations and structures, all immune-privileged compartments of the eye including cornea, ciliary body, and retina share the presence of specialized innate immune effectors, such as macrophages, that are involved in immune regulatory mechanisms (Shechter *et al*, 2013). In general, local tissue macrophages are considered as the key regulators ensuring proper tissue homeostasis and immune defense (Varol *et al*, 2015; Prinz *et al*, 2019).

Unlike microglia and CNS macrophages (MΦ) at interfaces like perivascular (pv), choroid plexus (cp), and meningeal (m) MΦ, which are derived from yolk sac precursors before birth (Ginhoux *et al*, 2010; Schulz *et al*, 2012; Kierdorf *et al*, 2013a; Goldmann *et al*, 2016; Kierdorf *et al*, 2019; Jordão *et al*, 2019), the macrophages found in the cornea, ciliary body, and even the retina were described to originate from short-lived blood monocytes after birth that are quickly replaced by bone marrow (BM)-derived cells (Xu *et al*, 2007; Kezic *et al*, 2008; Chinnery *et al*, 2008). These assumptions were made on the basis of immunohistochemical (Hume *et al*, 1983) or electron microscopy experiments (Gloor, 1969) that did not allow for longitudinal studies of labeled cells. The assumption of a postnatal origin of eye macrophages was also supported by the fact that retinal microglia increase in numbers around birth and during the first postnatal week (Santos *et al*, 2008). The systemic transplantation of genetically engineered BM-derived cells resulted in macrophage engraftment in the inner and outer plexiform layers, the ganglion cell layer and the optic nerve, but not in the photoreceptor layer of the retina (Boettcher *et al*, 2008). As these experiments used irradiation as conditioning paradigm and injection of BM cells that are not normally present in the circulation, the engraftment of BM cells in the preconditioned eye is likely a result of changes of the blood–ocular barrier and concomitant local induction of chemoattractants as described before for the brain (Mildner *et al*, 2007; Kierdorf *et al*, 2013b). Just recently, our knowledge about the origin and turnover of eye macrophages started to change. Using pulse labeling and fate mapping strategies, retinal microglia were shown to originate from the primitive hematopoiesis in the yolk sac while the origin of other macrophages in the eye remains unknown (O'Koren *et al*, 2019). Additionally, retinal microglia as well as macrophages in the iris/ciliary body were suggested to be long-lived whereas macrophages in the choroid and optic nerve showed a time-dependent turnover (O'Koren *et al*, 2019). Interestingly, depleted retinal microglia can be partially replenished by ciliary body macrophages *ex vivo* (Huang *et al*, 2018). Therefore, it is of interest to identify the origin of eye macrophages beside retinal microglia and understand the sources, kinetics, and functions of the myeloid subsets in the eye during health and disease in detail. From a functional point of view, macrophages in the cornea were found to balance the inflammatory response and wound healing after damage (Liu *et al*, 2017). Retinal microglia are essential to maintain a functional integrity of the retina (Wang *et al*, 2016). Consequently, a disturbed homeostasis of these cells is associated with neurodegeneration (Ma *et al*, 2019). Notably, patients suffering from age-related macular degeneration (AMD) display impaired retinal integrity with local myeloid cell activation and accumulation surrounding choroidal neovascularization (CNV), which can be modeled in rodents, e.g., in the laser-induced CNV model (Oh *et al*, 1999). This model covers important features of neovascular AMD found in patients, namely the sprouting of new choroidal vessels preceded by an activation of the resident innate immune system. However, so far the differential functions of resident retinal microglia vs. recruited monocytes and their underlying context-dependent functions during the development of CNV remain poorly defined due to the lack of appropriate cell-specific *in vivo* models.

In this study, a combination of single-cell RNA sequencing (scRNA-seq), embryonic and adult cell fate mapping, parabiosis, and use of reporter mouse lines allowed us to thoroughly compare the transcriptional profiles, origin and turnover characteristics of retinal microglia, and resident macrophages in the ciliary body and cornea. In addition, in a model of CNV, we were able to identify new disease-associated myeloid subpopulations that may represent a novel target for the treatment of AMD.

Results

Molecular survey of myeloid populations in the eye

The eye shows a remarkable anatomical compartmentalization reflecting the multimodal functions of the ocular visual system (Fig 1A). To comprehensively characterize the myeloid cells in the eye, we first asked how transcriptionally similar retinal microglia (rMG), ciliary (cbMΦ), and corneal macrophages (cMΦ) are. For this purpose, we purified the $CD45^+CD3^-CD19^-Ly6G^-$ cell fractions from the carefully dissected and separated cornea, ciliary body, and retina for morphological examination in parallel to scRNA-seq of the sorted cells as described before (Jordão *et al*, 2019; Masuda *et al*, 2019; Sankowski *et al*, 2019). In the retina, we consistently found smaller $CD45^+CD3^-CD19^-Ly6G^-$ myeloid cells with basophilic cytoplasm, while cells in the ciliary body and cornea showed a classical macrophage/monocyte appearance (Fig 1B). The morphological diversity of myeloid cells in the investigated eye compartments was also reflected in our scRNA-seq results that allowed us to clearly distinguish between microglia, macrophages, and a minor proportion of periphery-derived leukocytes as shown before (Jordão *et al*, 2019; Sankowski *et al*, 2019) (Fig 1C). We performed the mCel-Seq2 protocol followed by analysis using the RaceID3 algorithm (Herman *et al*, 2018). After the exclusion of contaminating cells consisting of neuronal cells from the retina and epithelial cells mostly from the cornea (Fig EV1), we identified 17 distinct clusters using the *t*-distributed stochastic neighbor embedding (*t*-SNE) algorithm. Here, we found either microglial (three clusters), macrophage (nine clusters), or peripheral leukocyte gene expression signatures (five clusters) based on previously described cell type-associated genes (Jordão *et al*, 2019) (Fig 1D). These clusters were differently enriched in the distinct compartments (Fig 1E and F). Clusters 13, 14, and 15 were exclusively derived from the retina and represent three distinct transcriptional cell states. As an example, cluster 13 shows the highest expression of cathepsin S and D (*Ctss, Ctsd*) suggesting active processing of phagocytosed antigen reflected by the presence of photoreceptor genes (*Rho, Gnat1*). The clusters 2, 3, 6, 9, and 16 were significantly enriched in the cornea and the clusters 1, 5, 10, 11, and 12 in the ciliary body based on hypergeometric testing with a cutoff of adjusted *P*-value <0.05 (Fig 1F).

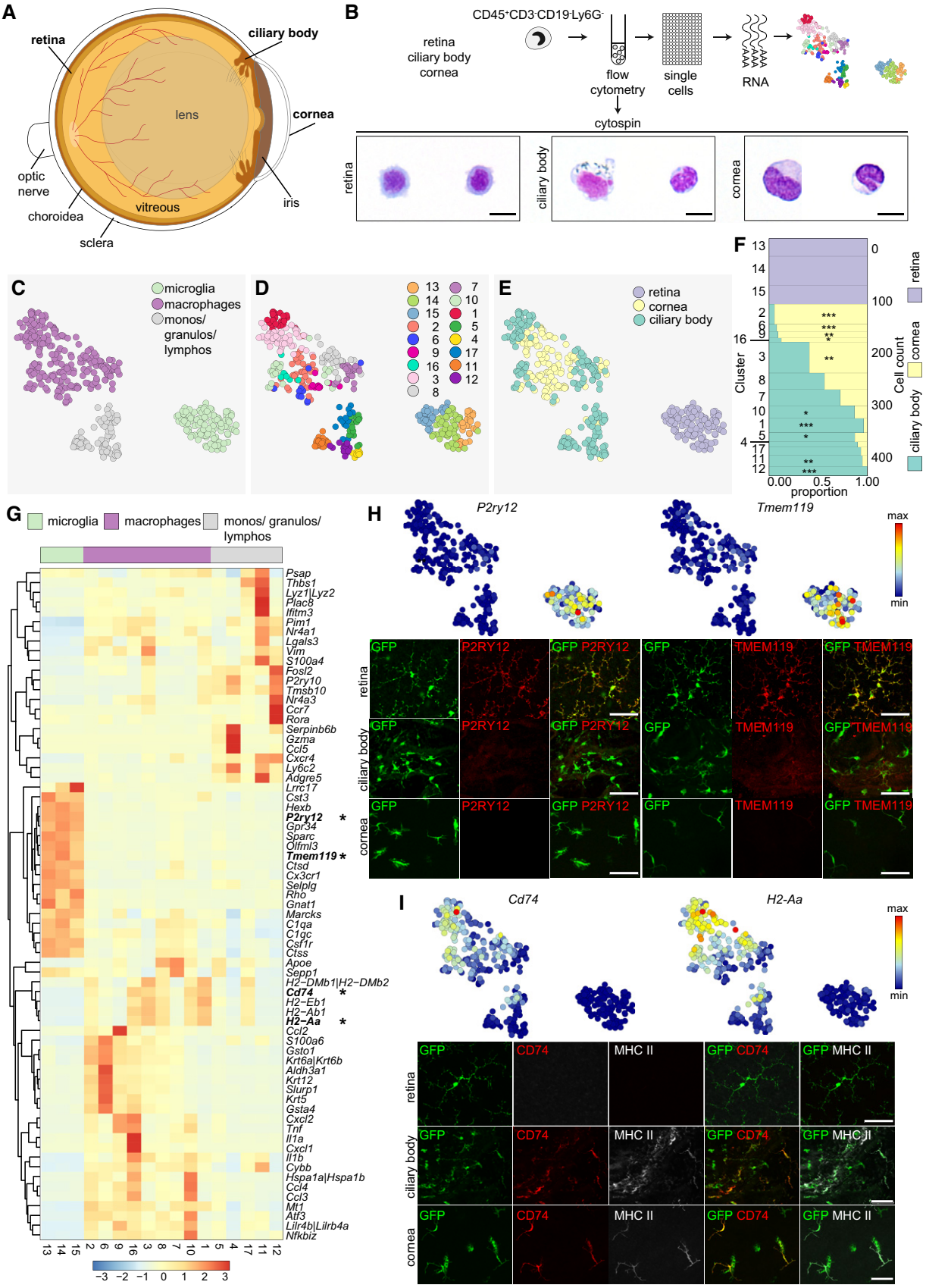
A
retina
ciliary body
lens
cornea
optic nerve
vitreous
iris
choroidea
sclera
B
CD45+CD3-CD19-Ly6G-
retina
ciliary body
cornea
flow cytometry
single cells
RNA
cytospin
retina
ciliary body
cornea
C
microglia
macrophages
monos/ granulos/ lymphos
D
13 14 15 2 6 9 16 3 8
7 10 1 5 4 17 11 12
E
retina
cornea
ciliary body
F
Cluster
Cell count
proportion
retina
cornea
ciliary body
G
microglia
macrophages
monos/ granulos/ lymphos
Psap
Thbs1
Lyz1|Lyz2
Plac8
Ifitm3
Pim1
Nr4a1
Lgals3
Vim
S100a4
Fosl2
P2ry10
Tmsb10
Nr4a3
Ccr7
Rora
Serpinb6b
Gzma
Ccl5
Cxcr4
Ly6c2
Adgre5
Lrrc17
Cst3
Hexb
P2ry12 *
Gpr34
Sparc
Olfml3
Tmem119 *
Ctsd
Cx3cr1
Selplg
Rho
Gnat1
Marcks
C1qa
C1qc
Csf1r
Ctss
Apoe
Sepp1
H2-DMb1|H2-DMb2
Cd74 *
H2-Eb1
H2-Ab1
H2-Aa *
Ccl2
S100a6
Gsto1
Krt6a|Krt6b
Aldh3a1
Krt12
Slurp1
Krt5
Gsta4
Cxcl2
Tnf
Il1a
Cxcl1
Il1b
Cybb
Hspa1a|Hspa1b
Ccl4
Ccl3
Mt1
Atf3
Lilr4b|Lilrb4a
Nfkbiz
13 14 15 2 6 9 16 3 8 7 10 1 5 4 17 11 12
−3 −2 −1 0 1 2 3
H
P2ry12
Tmem119
max
min
retina
ciliary body
cornea
GFP
P2RY12
TMEM119
I
Cd74
H2-Aa
max
min
retina
ciliary body
cornea
GFP
CD74
MHC II

Figure 1.

Figure 1. Molecular census of myeloid cells in different compartments of the healthy mouse eye.

A Scheme of the murine eye.

B Schematic diagram depicting the workflow for the isolation of single $CD45^+CD3^-CD19^-Ly6G^-$ cells from different eye compartments (retina, ciliary body, cornea) under healthy conditions for unbiased single-cell RNA-seq (scRNA-seq). Morphological heterogeneity of sorted myeloid cells revealed by May-Grünwald-Giemsa stained cytospins. Scale bars represents 10 μm.

C *t*-SNE representation of individual hematopoietic cells from all eye compartments measured by scRNA-seq. Each dot represents an individual cell. Color code indicates the respective cell types.

D Unbiased cluster analysis of subpopulations of cells found in the steady-state adult retina (cluster 13, 14, 15), ciliary body (cluster 1, 5, 10, 11, 12), cornea (cluster 2, 3, 6, 9, 16) and of mixed composition (4, 7, 8, 17) could be identified as microglia (cluster 13, 14, 15), macrophages (cluster 1, 2, 3, 6, 7, 8, 9, 10, 16), or peripheral blood leukocytes (cluster 4, 5, 11, 12, 17).

E *t*-SNE representation of single cells based on the tissue of origin.

F Stacked bar plot (Marimekko chart) representation of macrophage subsets to a given cluster demonstrating pure microglia populations in clusters 13, 14, and 15. Hypergeometric testing revealed significantly enriched macrophage clusters in the cornea (2, 3, 6, 9, 16) and the ciliary body (1, 5, 10, 11, 12) as indicated by asterisks ($*P < 0.05$, $**P < 0.01$, $***P < 0.001$).

G Heatmap of the most regulated genes per cluster (adjusted *P*-value < 0.05 based on the negative binomial distribution). Clusters are arranged from the left to the right and represent microglia (light green), macrophages (purple), and monocytes/granulocytes/lymphocytes (gray). The scale bar represents color-coded *z*-scores. Genes that were subsequently confirmed on protein level in (H) and (I) are highlighted by asterisks.

H Above: *t*-SNE representation of *P2ry12* and *Tmem119* expression. Below: immunofluorescence images for P2RY12 (red) and TMEM119 (red) in CX_3CR1^+ (green) retinal microglia (outer plexiform layer) but not in CX_3CR1^+ cells in the ciliary body and the peripheral stroma and epithelium of the cornea. Representative images out of three animals are shown. Scale bars represent 50 μm.

I Above: *t*-SNE plots for *Cd74* and *H2-Aa* expression. Below: Typical immunofluorescence pictures for CD74 (red) and MHCII (*H2-Aa*) (red) in CX_3CR1^+ (green) cells in the ciliary body and the peripheral stroma and epithelium of the cornea. Two animals were examined. Scale bars represent 50 μm.

Subsequent GO term analysis revealed functional similarities that were common in all compartments, e.g., "phagocytosis" or "mononuclear cell proliferation" (Fig EV2). Of note, other GO terms were only present in single clusters like "monoamine transport" in the rMG cluster 15 or "positive regulation of leukocyte tethering or rolling" in cluster 11, likely being monocytic cells, expressing *Plac8* and *Ly6c2* (Figs 1G and EV2). Transcripts known to be predominantly expressed by microglia (*Cx3cr1*, *P2ry12*, *Tmem119*, *Hexb*) were enriched in clusters 13, 14, and 15 of scRNA-seq data representing rMG (Fig 1G and H).

Next, we compared eye macrophages with brain macrophages (Jordão *et al*, 2019). We found that retinal and brain microglia are transcriptionally very similar by sharing a cluster (0) exclusively composed of brain- and retina-derived cells (Fig EV3A–D). Besides several clusters of mixed composition, three of them (3, 4, 5) appear to be significantly enriched with cells from the ciliary body by hypergeometric testing with no contribution from the retina (Fig EV3C). While the microglial cluster 0 clearly overlaps with the "microglia" signature plot, the ciliary body cluster 3 shows an association with the signature of "border-associated macrophages" and "monocytes" (Fig EV3E).

In line with that, our bulk RNA-seq analysis of brain microglia (bMG), rMG, bone marrow monocytes (BM-Mo), and cMΦ supported our findings of cell type-specific transcriptional profiles with rMG and bMG being transcriptionally similar (Fig 2). Comparative transcriptional profiling and principal component analysis (PCA) revealed that cMΦ were more comparable to BM-Mo and clearly separated from bMG and rMG, which both clustered together (Fig 2A–C). As expected, all examined myeloid subtypes expressed *Ptprc* (CD45), *Itgam* (CD11b), and *Csf1r* (CD115) (Fig 2D).

For protein validation of microglia- and macrophage-specific target genes, we used $Cx3cr1^{GFP/+}$ mice that harbor a targeted replacement of a *Cx3cr1* chemokine receptor allele with a cDNA encoding enhanced green fluorescence protein (eGFP) (Jung *et al*, 2000). In the healthy rodent brain, only microglia and CNS-associated macrophages (CAMs) such as pvMΦ, cpMΦ, and mMΦ express this marker (Goldmann *et al*, 2016; Hagemeyer *et al*, 2016). We were able to identify CX_3CR1^+ cells in different compartments of the eye but the expression of P2RY12 and TMEM119 was strictly limited to rMG, thereby confirming our scRNA- and bulk RNA-seq data (Figs 1G and H, and 2E). In contrast, genes involved in antigen presentation, such as *Cd74* and *H2-Aa*, encoding the alpha chain of the MHC class II protein, and the mannose receptor CD206 (*Mrc1*) were only expressed by macrophages on both transcriptional and protein levels, but absent in rMG (Figs 1G and I, and 2F and G). Next, we extended our validation experiments with fluorescent reporter mouse lines (Fig 2G). In *Itgax*-DTR-GFP mice, we detected a low fraction of $Iba1^+CD11c^+$ cells throughout the retina but also in the cornea, as described before (Hamrah *et al*, 2003; Dando *et al*, 2016; Fig 2G). In a novel $Hexb^{tdT/tdT}$ reporter mouse model, virtually all rMG were labeled but also cMΦ, to a certain extent underlining the common myeloid nature of these cell types despite their overall diverse expression signatures (Masuda *et al*, 2020; Fig 2G). Taken together, these data reveal the existence of heterogeneous myeloid subsets in the healthy eye, reflected by distinct morphology and transcriptional signatures validated by the corresponding protein expression.

Prenatal origin of eye macrophages in different compartments

In the past, the origin of myeloid cells in the eye was mainly investigated by the use of lethally irradiated mice undergoing BM transplantation to follow the fate of blood-derived myeloid cells as a putative source of rMG (Xu *et al*, 2007; Boettcher *et al*, 2008), cMΦ (Chinnery *et al*, 2008; Liu *et al*, 2017), and cbMΦ (Kezic *et al*, 2008). We were able to recapitulate these findings and found donor-derived $Iba1^+GFP^+$ rMG mostly in the inner plexiform layer (IPL) of irradiated wild-type hosts that received BM cells from $Acta1^{GFP/+}$ mice (Fig 3A–D).

In several organs, including the brain, resident macrophages arise from embryonic precursors in the yolk sac or fetal liver that seed the tissue before birth (Schulz *et al*, 2012; Yona *et al*, 2013; Kierdorf *et al*, 2013a; Molawi *et al*, 2014; Goldmann *et al*, 2016; Hagemeyer *et al*, 2016; Ensan *et al*, 2016). In order to circumvent

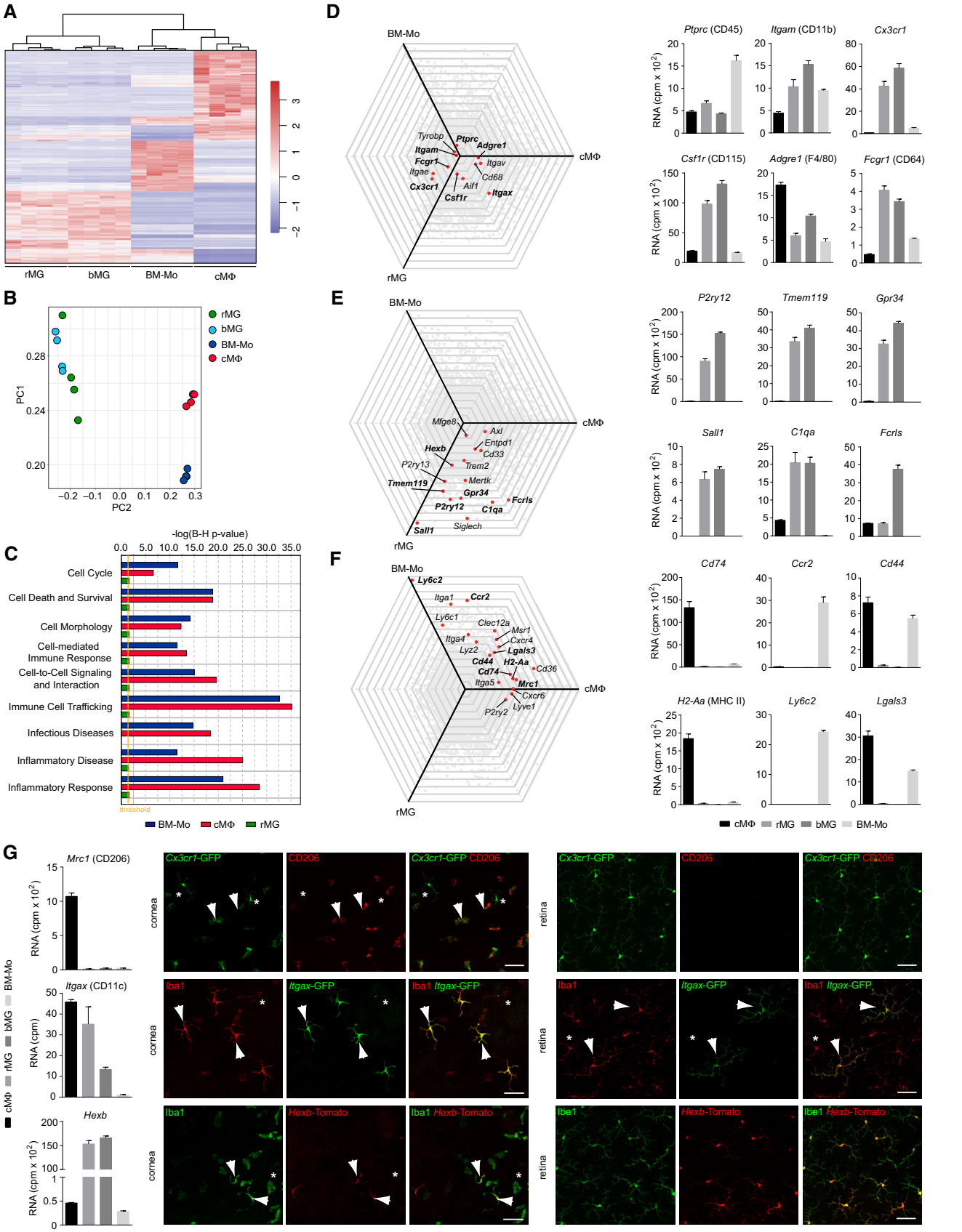
A
rMG
bMG
BM-Mo
cMΦ
B
PC1
PC2
C
-log(B-H p-value)
Cell Cycle
Cell Death and Survival
Cell Morphology
Cell-mediated Immune Response
Cell-to-Cell Signaling and Interaction
Immune Cell Trafficking
Infectious Diseases
Inflammatory Disease
Inflammatory Response
threshold
D
E
F
Ptprc (CD45)
Itgam (CD11b)
Cx3cr1
Csf1r (CD115)
Adgre1 (F4/80)
Fcgr1 (CD64)
P2ry12
Tmem119
Gpr34
Sall1
C1qa
Fcrls
Cd74
Ccr2
Cd44
H2-Aa (MHC II)
Ly6c2
Lgals3
RNA (cpm x 10²)
G
Mrc1 (CD206)
Itgax (CD11c)
Hexb
RNA (cpm)
cornea
retina
Cx3cr1-GFP
CD206
Iba1
Itgax-GFP
Hexb-Tomato

Figure 2.

Figure 2. Comparative bulk RNA-seq analysis of microglia from brain and retina, cornea macrophages, and bone marrow-derived monocytes.

A Heatmap of differentially expressed genes between rMG, bMG, cMΦ, or bone marrow-derived monocytes (BM-Mo). The mean centered and s.d. scaled expression values for genes that were significantly and at least twofold more or less abundantly expressed are shown. See Fig EV4 for gating strategy. Data are derived from four independent experiments with 5–10 pooled mice per sample and shown as mean ± s.e.m.

B Principal component analysis of myeloid cell transcripts analyzed by RNA-seq. Data are derived from four independent experiments with 5–10 pooled mice per sample and shown as mean ± s.e.m.

C Comparison of functional gene clusters between BM-Mo, cMΦ, and rMG in comparison with bMG (reference population). Data are derived from four independent experiments with 5–10 pooled mice per sample and shown as mean ± s.e.m.

D Left, spider plots showing commonly expressed genes across macrophages in comparison with bMG (reference population, center). Bold genes were plotted as bar graph on the right. Four samples were analyzed per cell type. Data are derived from four independent experiments with 5–10 pooled mice per sample and shown as mean ± s.e.m.

E Left, spider plots showing genes highly enriched in microglia in comparison with bMG (reference population, center). Bold genes are plotted as bar graphs on the right. Data are derived from four independent experiments with 5–10 pooled mice per sample and shown as mean ± s.e.m.

F Left, spider plots showing genes commonly expressed by monocytes and/or cMΦ in comparison with bMG (reference population, center). Bold genes are plotted as bar graphs (right). Data are derived from four independent experiments with 5–10 pooled mice per sample and shown as mean ± s.e.m.

G Left, bar graphs showing expression of the genes *Mrc1*, *Itgax*, and *Hexb* in rMG, bMG, cMΦ, or bone marrow-derived monocytes (BM-Mo). Right, validation of *Mrc1* (CD206) in *Cx3cr1*-GFP mice, *Itgax* in *Itgax*-GFP mice, and *Hexb* in *Hexb*-Tomato mice in the cornea and the retina. Arrows point to $CX_3CR1^+CD206^+$ cMΦ (top row) or $Iba1^+CD11c^+$ cMΦ or rMG (middle row) or $Iba1^+Hexb^+$ cMΦ or rMG (bottom row). Asterisks point $CX_3CR1^+CD206^-$ cMΦ (top row) or $Iba1^+CD11c^-$ cMΦ or rMG (middle row) or $Iba1^+Hexb^-$ cMΦ or rMG (bottom row). Data are derived from four independent experiments with 5–10 pooled mice per sample and shown as mean ± s.e.m. Scales bar represents 50 μm.

the irradiation-induced artifacts of BM chimeras, we used tamoxifen (TAM)-inducible *Cx3cr1*^{CreERT2}*:Rosa26-YFP* mice for the investigation of a potential prenatal origin of eye macrophages in an embryonic fate mapping approach as described before (Goldmann *et al*, 2016; Fig 3E–G). By doing so, it was possible to follow irreversibly recombined long-living $CX_3CR1^+YFP^+Iba1^+$ cells from embryonic day 9 (E9.0) to postnatal day 0 (P0) in the retina, ciliary epithelium, and the cornea (Fig 3F and G). At P0, $Iba1^+$ rMG showed the highest percentage of YFP^+ cells (51.36 ± 5.7%) among the investigated eye macrophage populations comparable to the labeling rates we have shown before for bMG and CAMs such as pvMΦ and mMΦ using a similar approach (Goldmann *et al*, 2016). Of note, rMG were described before to emerge from the yolk sac which was shown with the *Runx1-Mer-Cre-Mer* mouse model (O'Koren *et al*, 2019). In addition, we identified for the first time pulse-labeled cbMΦ (32.0 ± 8.8%) in the developing ciliary body, called ciliary epithelium, and cMΦ (22.26 ± 7.1%) in the cornea (Fig 3G). In conclusion, all investigated compartments of the murine eye contained macrophages (rMG, cbMΦ, and cMΦ) of prenatal origin that derive either from the yolk sac and/or the fetal liver to various degrees.

Different turnover of macrophage subsets in the healthy adult eye

Macrophages in the brain are located either inside the brain parenchyma like microglia or at CNS interfaces like CAMs (Kierdorf *et al*, 2019). These compartments are separated by the blood–brain barrier and, as a consequence, macrophages residing behind this barrier are long-lived and self-maintained with only limited random expansion under physiological conditions (Tay *et al*, 2017).

To investigate the turnover of macrophages in different compartments of the eye during steady state, we compared the turnover of rMG with cbMΦ and cMΦ in adult mice. At the age of 6 weeks, we injected *Cx3cr1*^{CreERT2}*:Rosa26-YFP* mice subcutaneously twice with TAM to specifically label long-living macrophages while short-lived myeloid cells like monocytes lose the label over time (Goldmann *et al*, 2013; Wieghofer *et al*, 2015). Next, we quantified the YFP expression in rMG, cbMΦ, and cMΦ at 2, 12, and 24 weeks after TAM administration (Fig 4A–C). Flow cytometry revealed long-term YFP expression of $CD45^+CD11b^+$ rMG (2 weeks: 91.54 ± 2.98%, 12 weeks: 92.13 ± 2.08%, 24 weeks: 96.30 ± 1.62%), which is reminiscent of the low turnover that has been described in the same model for bMG and CAMs such as pvMΦ and mMΦ (Goldmann *et al*, 2016). $CD45^+CD11b^+CD64^+F4/80^+$ cbMΦ also showed long-term YFP expression (2 weeks: 82.23 ± 6.33%, 12 weeks: 69.17 ± 7.33%, 24 weeks: 76.90 ± 5.18%) resembling previous results (O'Koren *et al*, 2019). In contrast, the percentage of YFP^+ cells among $CD45^+CD11b^+CD64^+F4/80^+$ cMΦ strongly dropped over time (2 weeks: 66.91 ± 7.10%, 12 weeks: 28.39 ± 4.31, 24 weeks: 17.32 ± 2.03%) comparable to the short-lived nature of choroidal macrophages (O'Koren *et al*, 2019).

In line with these results, *Flt3*^{Cre}*:Rosa26-YFP* mice, labeling all descendants from the definitive hematopoiesis, showed the highest recombination in cMΦ (12 weeks: 62.24 ± 5.92%, 52 weeks: 72.55 ± 2.6) but only low labeling in cbMΦ (12 weeks: 12.61 ± 0.2%, 52 weeks: 16.7 ± 4.1) that was virtually undetectable in rMG (12 weeks: 0.1 ± 0.04%, 52 weeks: 0.05 ± 0.03%) by flow cytometry (Fig 4D–F). Of note, *Flt3*^{Cre} mice are known to target also the prenatal definitive hematopoiesis in the fetal liver, beside the BM in adulthood (Perdiguero *et al*, 2014). We therefore aimed to confirm our findings from the *Cx3cr1*^{CreERT2}*:Rosa26-YFP* mice by exclusively targeting peripheral blood monocytes without a contribution of the fetal liver and without compromising the blood–ocular barriers as in irradiated BM chimeras. Subsequently, we generated parabiotic mice and analyzed them 2, 12, and 20 weeks after pairing of *Acta1*$^{GFP/+}$ with *Acta1*$^{+/+}$ mice (Fig 5A–D). Notably, we did not detect any GFP^+Iba1^+ rMG in the *Acta1*$^{+/+}$ partner and only low numbers in cbMΦ (2 weeks: 0.27 ± 0.18%, 12 weeks: 0.62 ± 0.31%) (Fig 5A–D). In contrast, the frequency of GFP^+Iba1^+ cMΦ coming from the parabiotic partner steadily increased over time (2 weeks: 0.46 ± 0.28%, 12 weeks: 5.62 ± 2.27%, 20 weeks: 11.30 ± 2.80%) confirming a contribution of blood-derived cells from the definitive hematopoiesis to this particular macrophage population (Fig 5A and D).

To gain more insight into the identity of the cell type in the peripheral blood contributing to the high turnover of cMΦ, we next

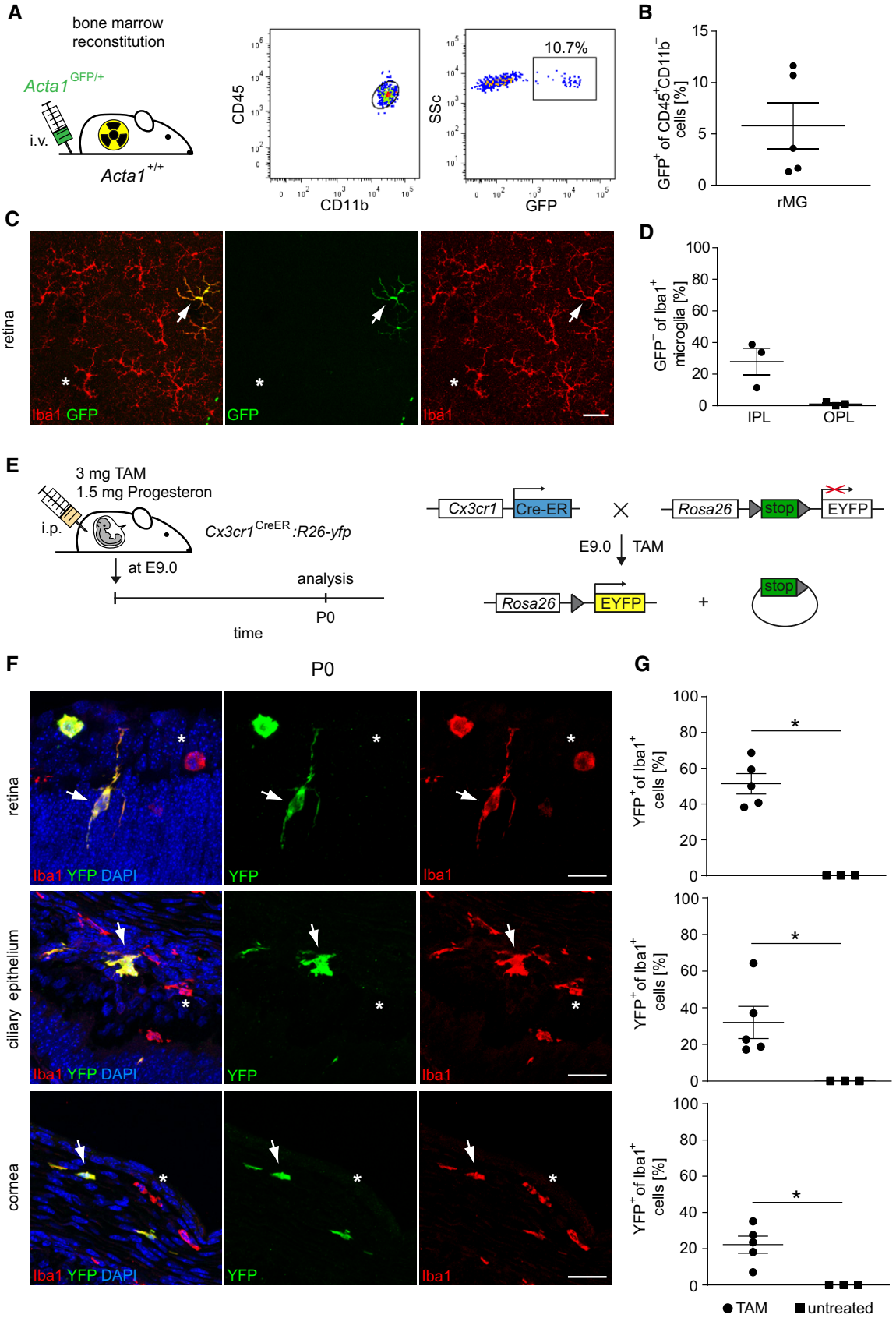
A
bone marrow reconstitution
Acta1 GFP/+
i.v.
Acta1 +/+
CD45
CD11b
SSc
GFP
10.7%
B
GFP+ of CD45+CD11b+ cells [%]
rMG
C
retina
Iba1 GFP
GFP
Iba1
D
GFP+ of Iba1+ microglia [%]
IPL
OPL
E
3 mg TAM
1.5 mg Progesteron
i.p.
Cx3cr1 CreER :R26-yfp
at E9.0
analysis
P0
time
Cx3cr1
Cre-ER
Rosa26
stop
EYFP
E9.0
TAM
F
P0
retina
ciliary epithelium
cornea
Iba1 YFP DAPI
YFP
Iba1
G
YFP+ of Iba1+ cells [%]
TAM
untreated

Figure 3.

Figure 3. Prenatal source of eye macrophages.

A Left: Creation of *Acta1*$^{GFP/+}$:*Acta1*$^{+/+}$ bone marrow chimeras. Right: Donor-derived GFP$^+$CD45^{lo}CD11b$^+$ were detectable in the recipient retina by flow cytometry 20 weeks after bone marrow reconstitution. FACS Plots are representative for five animals from one experiment.

B Quantification of GFP$^+$ cells among CD45$^+$CD11b$^+$ retinal microglia by flow cytometry. Data are presented as mean ± s.e.m. One symbol represents one mouse.

C Typical retinal flat mount from *Acta1*$^{GFP/+}$:*Acta1*$^{+/+}$ bone marrow chimeras 20 weeks after reconstitution. Donor-derived GFP$^+$Iba1$^+$ cells (arrow) and GFP$^-$Iba1$^+$ resident microglia (asterisks) are shown. Pictures are representative for three animals from one experiment. Scale bars represent 50 μm.

D Microscopy-based quantification of GFP$^+$Iba1$^+$ retinal microglia in the inner (IPL) and outer plexiform layer (OPL). One symbol represents one mouse. Data are presented as mean ± s.e.m.

E Scheme of a fate mapping experiment using *Cx3cr1*^{CreERT2}:*Rosa26-YFP* female mice. Tamoxifen (TAM) and progesterone injection were performed at embryonic day 9.0 (E9.0). Mice were subsequently evaluated at postnatal day 0 (P0). Administration of TAM leads to intra-embryonic excision of a stop sequence flanked by loxP sites (gray triangles) in *Cx3cr1* expressing cells which causes stable and steady YFP expression under the control of the *Rosa26* promotor.

F Direct fluorescence microscopic visualization for YFP (green), the macrophage marker Iba1 (red) and DAPI for the nuclei (blue) at P0. YFP$^+$Iba1$^+$ double-positive cells are marked by arrows. YFP$^-$Iba1$^+$ single-positive cells are labeled by asterisks. Representative images out of five examined animals are shown. Scale bars represent 25 μm.

G Quantitative analysis of regional YFP expression in Iba1$^+$ macrophages in TAM-induced and untreated *Cx3cr1*^{CreERT2}:*Rosa26-YFP* mice. Bars represent means ± s.e.m. Quantification was done from three (untreated) or five (TAM) mice obtained from one (untreated) or two (TAM) independent experiments. Level of significance determined by Mann–Whitney test between TAM and untreated revealed *$P < 0.05$ and Kruskal–Wallis test between retina, ciliary body, and cornea revealed *$P = 0.0204$.

investigated *Ccr2-RFP* mice, in which all short-lived CCR2$^+$ monocytes and their descendants express the red fluorescent protein (RFP) (Saederup *et al*, 2010; Fig 5E–I). Again, we did not detect any rMG and only few cbMΦ that expressed RFP by flow cytometry (4.93 ± 1.37%) (Fig 5E–H) or confocal microscopy (Fig 5J). In contrast, up to one third of cMΦ expressed RFP as quantified by flow cytometry (28.94 ± 2.96%) which is in line with previous reports (Liu *et al*, 2017) and our microscopical evaluation (Fig 5E, H and J). All circulating Ly6C^{hi} and Ly6C^{lo} monocytes expressed RFP serving as a positive control (Fig 5E and I) (Saederup *et al*, 2010). The low Cre recombination of rMG and cbMΦ in *Flt3*^{Cre}:*Rosa26-YFP* animals suggests that their development occurred largely independent of *Flt3*$^+$ multipotent hematopoietic precursors in the BM. On the contrary, the high turnover in *Cx3cr1*^{CreERT2}:*Rosa26-YFP* mice, the strong labeling in *Flt3*^{Cre}:*Rosa26-YFP* and *Ccr2-RFP* mice and the time-dependent increase of GFP$^+$ cells during parabiosis is strongly indicative of a role of hematopoietic stem cells in the maintenance of cMΦ.

In sum, these data clearly show different turnover kinetics of macrophages in distinct compartments of the healthy eye, namely that rMG and cbMΦ share their longevity with microglia and CAMs in the brain that have no or negligible input from blood monocytes. In contrast, cMΦ are characterized by a dual origin. They are initially composed of yolk sac-derived cells; however in adult mice, cMΦ are continuously replaced with cells derived from the definitive hematopoiesis with a short turnover.

Spatial and temporal distribution of myeloid cell subsets during the formation of choroidal neovascularization

To investigate the kinetics of myeloid cell subsets and the appearance of disease-associated cell populations during retinal pathology, we used a model of experimental CNV. This model is characterized by the formation of new vessels, which mimics the main hallmark of neovascular AMD in humans. For this purpose, CNV was induced by laser treatment in *Cx3cr1*^{CreERT2}:*Rosa26-tdTomato* mice 8 weeks after TAM treatment (Fig 6A). *In vivo* funduscopic imaging of untreated non-lesioned mice revealed no signs of retinal damage and tomato$^+$ rMG were evenly distributed in the retina (Fig 6B). Notably, the corresponding retinal pigment epithelium (RPE) was devoid of any Iba1$^+$tomato$^+$ myeloid cells in non-lesioned mice (Fig 6B). At 7 days after laser treatment, laser-induced lesions were clearly apparent and tomato$^+$ rMG were increased at the lesion site (Fig 6C). In parallel, fluorescence angiography showed a marked leakage of fluorescein caused by the newly formed immature vessels (Fig 6C). The cellular composition of infiltrating cells changed dramatically after laser-induced CNV formation in comparison with the control mice. First, Iba1$^+$tomato$^+$ rMG in the retina were morphologically altered with fewer ramifications and Iba1$^+$tomato$^-$ recruited macrophages entered the lesioned eye (Fig 6C). Second, the lesion site at the level of the RPE was infiltrated by resident amoeboid Iba1$^+$tomato$^+$ rMG and by Iba1$^+$tomato$^-$ recruited macrophages, likely of monocytic origin as suggested by a loss of tomato in peripheral blood monocytes. We next performed semi-automatic IMARIS-based image quantification to assess the proportions and kinetics of different myeloid cell subsets during CNV in the whole confocal stack volume of single lesions (Fig 6D and E). In the retina, the percentage and number of Iba1$^+$tomato$^+$ rMG were strongly increased during pathology with minimal engraftment by peripheral monocytes while both Iba1$^+$tomato$^-$ recruited macrophages and Iba1$^+$tomato$^+$ rMG were present in the RPE (Fig 6D and E). To confirm a sufficiently high recombination in rMG, we performed flow cytometry and found virtually all CD45$^+$CD11b$^+$ rMG to be positive for tomato (98.75 ± 1.18%) after TAM treatment and only negligible tomato expression in circulating CD45$^+$CD11b$^+$CD115$^+$SSc^{lo}Ly6C^{hi} (0.02 ± 0.02%) and CD45$^+$CD11b$^+$CD115$^+$SSc^{lo}Ly6C^{lo} (1.4 ± 0.24%) monocytes, suggesting specific and permanent labeling of long-lived CX$_3$CR1$^+$ macrophages in the eye (Boeck *et al*, 2020; Fig 6F). In addition, we would like to stress that TAM-independent recombination events occur specifically in tomato reporter mice and were present in around 50% of the CD45$^+$CD11b$^+$ rMG population, as reported before (Chappel-Maor *et al*, 2020). However, peripheral blood monocytes were not affected and consequently due to their short-lived nature no interference with our experimental setup occured (Fig 6G). In conclusion, we identified rMG emerging as the dominant myeloid cell subset present during CNV formation.

Identification of myeloid subpopulations associated with choroidal neovascularization

In order to analyze the diversity of myeloid cells on a single-cell level during pathology, we induced CNV by laser treatment in

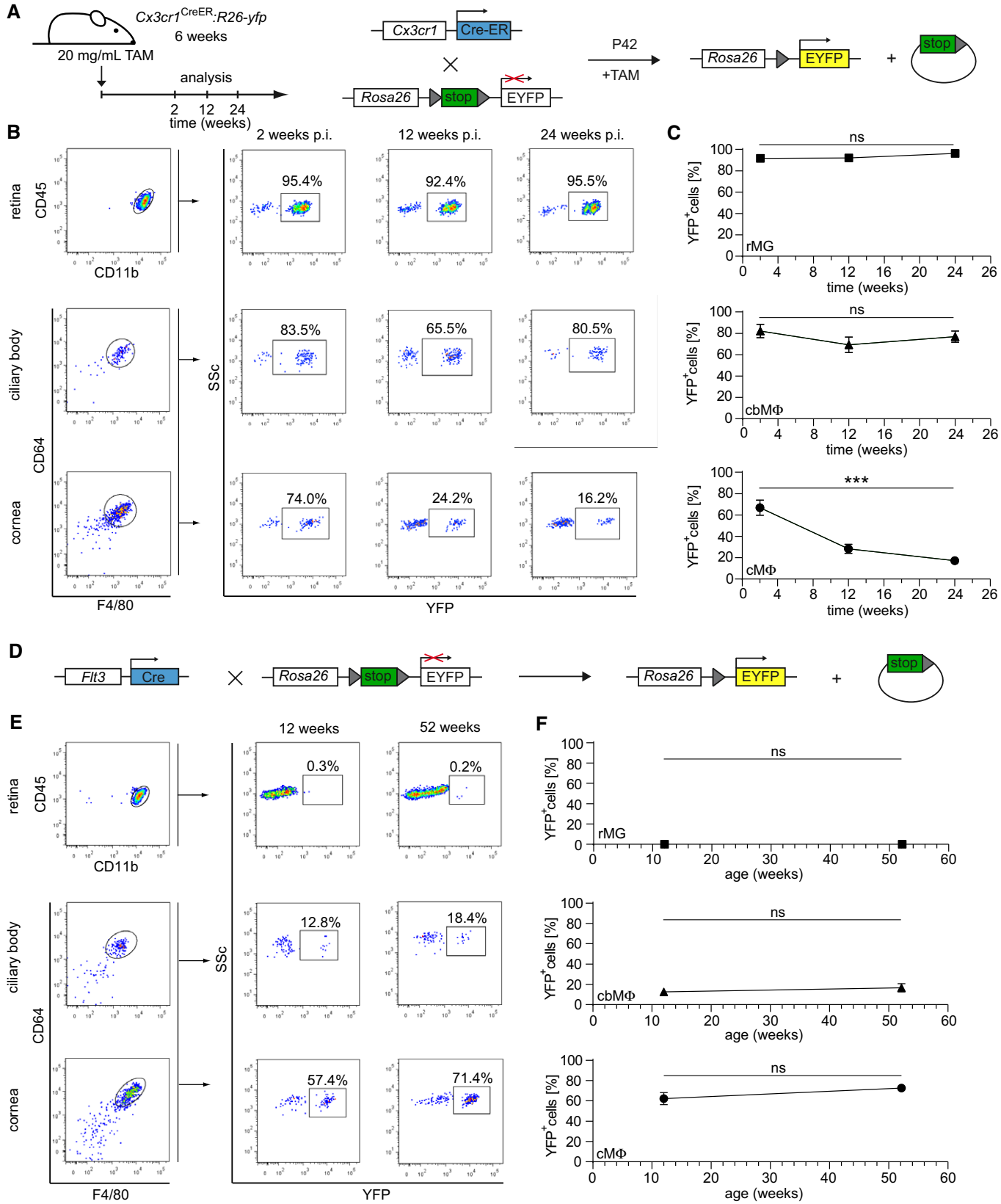
A
Cx3cr1CreER:R26-yfp
6 weeks
20 mg/mL TAM
analysis
2 12 24
time (weeks)
Cx3cr1
Cre-ER
Rosa26
stop
EYFP
P42
+TAM
B
2 weeks p.i.
12 weeks p.i.
24 weeks p.i.
retina
ciliary body
cornea
CD45
CD11b
CD64
F4/80
SSc
YFP
95.4%
92.4%
95.5%
83.5%
65.5%
80.5%
74.0%
24.2%
16.2%
C
YFP+cells [%]
rMG
cbMΦ
cMΦ
ns
***
time (weeks)
D
Flt3
Cre
E
12 weeks
52 weeks
0.3%
0.2%
12.8%
18.4%
57.4%
71.4%
F
age (weeks)

Figure 4.

Figure 4. Contribution of definitive hematopoiesis to eye macrophage subsets during steady-state.

A Scheme of a fate mapping experiment using adult *Cx3cr1*^{CreERT2}:*Rosa26-YFP* mice. Tamoxifen (TAM) injection was performed at postnatal day 42 (P42). Mice were evaluated at 2, 12, and 24 weeks post-injections. Administration of TAM leads to the excision of a stop sequence flanked by loxP sites (gray triangles) in *Cx3cr1* expressing cells in the eye which causes stable YFP expression under the control of the *Rosa26* promotor.

B Flow cytometric measurement of the persistence of YFP$^+$ retinal microglia (rMG), ciliary body (cb) MΦ, and corneal (c) MΦ in adult *Cx3cr1*^{CreERT2}:*Rosa26-YFP* mice. Doublets and dead cells were excluded by FSC-W and viability dye. Representative flow cytometry plots from two independent experiments with at least six mice are displayed.

C Kinetics of YFP labeling in macrophages of the healthy eye. Symbols represent means ± s.e.m. rMG are shown as squares (2 weeks: $n = 10$ mice, 12 weeks: $n = 9$ mice, 24 weeks: $n = 12$ mice, Kruskal–Wallis ns $P > 0.05$), cbMΦ are depicted as triangles (2 weeks: $n = 4$ samples from eight mice, 12 weeks: $n = 3$ samples from six mice, 24 weeks: $n = 6$ samples from twelve mice, Kruskal–Wallis ns $P > 0.05$) and cMΦ as circles (2 weeks: $n = 6$ mice, 12 weeks: $n = 8$ mice, 24 weeks: $n = 12$ mice, one-way ANOVA ***$P < 0.0001$). Data were obtained from two (cMΦ: 2 weeks, cbMΦ: 2 and 12 weeks), three (rMG: 2 weeks, cbMΦ: 24 weeks), or four (rMG: 12 and 24 weeks, coMΦ: 12 and 24 weeks) independent experiments.

D Sketch of the *Flt3*-dependent Cre-mediated recombination system with excision of the loxP-flanked stop-sequences leading to expression of YFP under the control of the *Rosa26* promotor in *Flt3*^{Cre}:*Rosa26-YFP* mice.

E Left: Representative flow cytometric characterization of rMG by CD45 and CD11b and cbMΦ and cMΦ by CD45, CD11b, CD64, and F4/80 in *Flt3*^{Cre}:*Rosa26-YFP* mice. Doublets and dead cell were excluded. Right: representative flow cytometric images depicting YFP expression in eye tissue macrophages of 12- or 52-week-old *Flt3*^{Cre}:*Rosa26-YFP* mice. Typical images were taken from two independent experiments with six to seven mice.

F Quantification of the percentage of YFP$^+$ eye macrophages at 12 and 52 weeks of age. rMG are shown as squares (12 weeks: $n = 7$ mice, 52 weeks: $n = 6$ mice), cbMΦ as triangles (12 weeks: $n = 3$ samples from six mice, 52 weeks: $n = 3$ samples from six mice), and cMΦ as circles (12 weeks: $n = 7$ mice, 52 weeks: $n = 6$ mice). Data are presented as means ± s.e.m. and were acquired in two independent experiments.

8-week-old C57BL/6J mice and used non-lesioned littermates as controls. We FACS-sorted CD45$^+$CD3$^-$CD19$^-$Ly6G$^-$ cell fractions of the carefully excised central part of the retina enriched with lesioned tissue at days 3 and 7 to perform scRNA-seq and compare it to homeostatic retinal microglial cells (Figs 1 and 7A). Cytospins revealed typical myeloid morphologies of isolated cells (Fig 7B). Contaminating neuronal retinal cells were again excluded from subsequent analysis (Fig EV5). Using the *t*-SNE algorithm (Fig 7C–E), we visualized several clusters that were only present in the CNV-related conditions (clusters 1, 7, 9, 10, 12, 13, 14) while others (4 and 5) were mostly consisting of cells derived from the homeostatic control time point d0 (Fig 7C).

Based on the expression of previously described cell type-enriched gene expression signatures (Jordão *et al*, 2019), we identified microglia and dendritic cells (DC), as well as other myeloid cells such as macrophages and peripheral blood-derived monocytes, among all assigned cells (Fig 7D). Only few cells could not be assigned to a certain cell type which represents a methodological limitation due to transcriptionally similar (myeloid) cells (Fig 7D). To clearly correlate the clusters to the control and diseased stages, we performed hypergeometric testing and confirmed a significant enrichment of cells derived from different conditions in specific clusters (Fig 7F). Besides the clusters related to the control (cluster 4, 5), we identified several disease-associated clusters related to the CNV d3 (cluster 1, 6, 7) and CNV d7 (cluster 11, 12, 14) time point (Fig 7F). The contribution of the different (assigned) cell types to the different stages showed the highest diversity at CNV d3 (Fig 7D and G).

The clusters 4 and 5 were characterized by a high expression of previously reported microglia signature genes, such as *Hexb, C1qa, and Sparc* (Gautier *et al*, 2012; Butovsky *et al*, 2014; Fig 7H and I). In contrast, cluster 6 was the only disease-associated rMG cluster found to be exclusively associated with CNV d3 and showed a "response to wounding" in the GO term analysis underlining its activated state (Fig EV6). In addition, this cluster shows a lower relative abundance of expression of the microglia signature genes typically expressed under homeostatic conditions, like *Gpr34* and *Csf1r*, but a relatively high expression of *Gapdh* suggesting an increased glycolytic activity eventually due to local hypoxia (Fig 7H and I). The heterogeneous expression pattern of Clusters 9 and 14 showed up-regulated genes commonly expressed by both macrophages and photoreceptor cells (*Pdegb, Cnga1, Gnat1*) indicating active phagocytosis of photoreceptor cell debris after laser coagulation (Fig 7H). Despite the presence of photoreceptor cell-related genes, cluster 14 was assigned as macrophage, according to our cell type-enriched gene expression signatures (Jordão *et al*, 2019) and expresses genes included in the GO term "phagocytosis", in addition to genes involved in antigen presentation (*H2-Aa, Cd74*), interferon response (*Ifitm1, Ifitm3*), and oxidative stress (*Gpx1*) (Figs 7H and I, and EV6). DCs also expressed genes typical for antigen presentation including *Cd74* and *H2-Aa*, encoding MHC class II, but to a much higher degree than macrophages (Fig 7H and I). In addition, the C-type lectin *Clec10a* supports the DC identity of these cells besides other genes (Fig 7I). The expression of *Ly6c2*, *Plac8,* and *Ms4a4b* was only found in clusters consisting of lymphocytes, monocytes, and granulocytes (Fig 7H and I). Taken together, our single-cell profiling identified rMG and myeloid cell cluster associated with choroidal neovascularization, suggesting that homeostatic subsets of endogenous rMG are able to quickly change their phenotypes and generate context- and time-dependent states. Notably, the novel disease-associated rMG clusters were still transcriptional distinct from cbMΦ and cMΦ.

Pseudotemporal ordering of the transcriptional dynamics during the course of neovascularization

To gain more insights into the gradual transcriptional changes in rMG during choroidal neovascularization, we performed a trajectory analysis using Monocle. This enabled us to identify transcriptionally different gene modules beyond the relative expression changes of single signature genes across clusters. We set up the algorithm to examine transcriptional changes between control, CNV d3, and CNV d7 cells of the microglial and macrophage clusters 3, 4, 5, 6, 11, and 14 and identified three gene modules (Fig 8A). The first module was enriched with control cells and characterized by the expression of microglial genes, like *Csf1r*, *Siglech*, *Tgfbr1*, and *Cx3cr1*. The second module was enriched with CNV d3 cells and characterized by the expression of genes encoding proteins associated with cytoskeleton

reorganization (*Actb*, *Tuba1c*, *Tmsbx4*) and proliferation (*Ptma*, *Pcna*, *Cdk1*). The third module was enriched for CNV d7 cells, and included genes underlying a more diverse regulation pattern, like *Sparc*, and the genes *Ctss*, *Cd74*, and *H2-Aa*, typically expressed by APC's. As shown in the minimum spanning tree, CNV d3 represented the acute phase after lesion formation while CNV d7 consisted of cells expressing macrophage-associated genes and was more similar to the non-lasered control mice indicating an overall

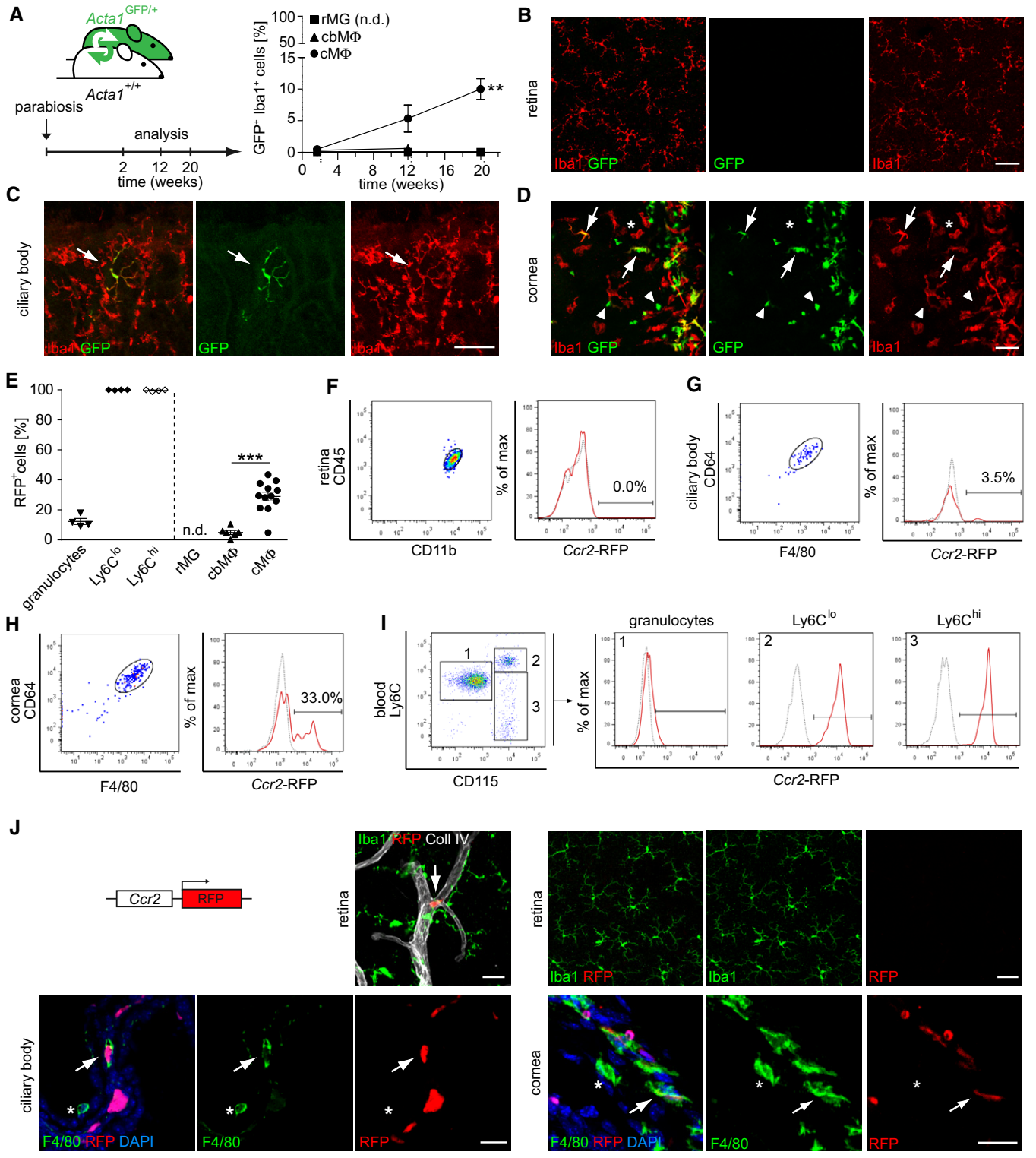

Figure 5.

Figure 5. Peripheral blood-derived origin of myeloid cells contributing to homeostatic turnover of eye macrophages.

A Left, Experimental setup of surgically connected parabiotic mice. *Acta1*$^{GFP/+}$ and *Acta1*$^{+/+}$ mice underwent parabiosis for 2, 12, and 20 weeks before analysis. Right, quantification of GFP$^+$Iba1$^+$ microglia in the retina (rMG, squares, n.d. = not detectable), ciliary body (cbMΦ, triangles, Mann–Whitney ns $P > 0.05$), and cornea (cMΦ, circles, Kruskal–Wallis $^{**}P = 0.0024$) of parabiotic mice. Blood chimerism of CD45$^+$CD11b$^+$Ly6C^{hi}GFP$^+$ cells in the analyzed wild-type mice was 37.7 ± 3.2% (2 weeks), 27.5 ± 2.7% (12 weeks), and 34.7 ± 3.7% (20 weeks). Symbols represent mean ± s.e.m. of three (2 weeks), four (12 weeks) or five (20 weeks) individual mice. Scale bars represent 50 μm.

B–D Representative immunofluorescence images from the retina (20 weeks), ciliary body (12 weeks), and cornea (20 weeks) from flat mounts of *Acta1*$^{+/+}$ parabiotic mice. GFP$^+$Iba1$^+$ double-positive cells are marked by arrows, GFP$^-$Iba1$^+$ single-positive cells are labeled by asterisks and GFP$^+$Iba1$^-$ leukocytes are indicated by arrow heads. Pictures are representative of three animals.

E Flow cytometric quantification of RFP$^+$ cells in *Ccr2-RFP* mice among CD45$^+$CD11b$^+$CD115$^-$Ly6C^{int} granulocytes (triangles, $n = 4$), CD45$^+$CD11b$^+$CD115$^+$Ly6C^{lo} monocytes (filled squares, $n = 4$ mice), CD45$^+$CD11b$^+$CD115$^+$Ly6C^{hi} monocytes (open squares, $n = 4$ mice), CD45^{lo}CD11b$^+$ rMG (squares, $n = 6$ mice), CD45$^+$CD11b$^+$CD64$^+$F4/80$^+$ cbMΦ (triangles, $n = 6$ samples from 12 mice), and CD45$^+$CD11b$^+$CD64$^+$F4/80$^+$ cMΦ (filled circles, $n = 12$ mice, unpaired *t*-test $^{***}P < 0.0001$). Data were obtained from one (rMG) or two independent experiments (blood, cbMΦ, cMΦ). Data are presented as means ± s.e.m.

F–H Flow cytometry of eye macrophages from healthy *Ccr2*$^{RFP/+}$ mice (left) and representative histograms (right, *Ccr2*$^{RFP/+}$ solid red line, *Ccr2*$^{+/+}$ controls dotted gray line).

I Flow cytometry of myeloid blood cells from *Ccr2*$^{RFP/+}$ mice. Left: CD45$^+$CD11b$^+$ cells were further subdivided according to the expression of Ly6C and CD115 into CD45$^+$CD11b$^+$CD115$^-$Ly6C^{int} granulocytes (gate 1), CD45$^+$CD11b$^+$CD115$^+$Ly6C^{hi} inflammatory (gate 2), and CD45$^+$CD11b$^+$CD115$^+$Ly6C^{lo} resident monocytes (gate 3), respectively. Right: representative histograms are shown (*Ccr2*$^{RFP/+}$ solid red line, *Ccr2*$^{+/+}$ controls dotted gray line). Four mice were investigated.

J Top left, sketch of *Ccr2-RFP* construct. Top right, typical confocal picture for CCR2 (red), Iba1 (green), and collagen IV (Coll IV, white) revealing *Ccr2-RFP* expression in a blood vessel (arrow, left image, scale bar represents 20 μm) and no RFP signal in retinal microglia (right images, scale bar represents 100 μm). Bottom, representative pictures of the ciliary body and cornea immunolabeled with F4/80 (green), CCR2 (red), and DAPI (blue). Arrows indicate RFP$^+$F4/80$^+$ cells. Asterisks point to RFP$^-$F4/80$^+$ cells. Representative images from two independent experiments with three mice are displayed. Scale bars represents 20 μm.

decline in myeloid cell reactivity (Figs 8A and 7G). Despite the presence of diverse cell types in the CNV-lesioned areas, microglia represent the most abundant cell type at all investigated time points after lesion formation (Figs 6D and E, and 7D and G).

Next, we took advantage of *Cx3cr1*^{CreERT2}*:Rosa26-tdTomato* mice to validate the down-regulation of P2RY12 and TMEM119 and the presence of microglial proliferation indicated by the up-regulation of the *proliferating cell nuclear antigen* (*Pcna*) and *prothymosin alpha* (*Ptma*) (Fig 8B–D). Both *P2ry12* and *Tmem119* expression decreased with disease progression and could only be detected in the clusters 3, 4, and 5, but was lost in cluster 6 (Fig 8B and C). At CNV d7, highly ramified tomato$^+$P2RY12$^+$ microglial cells were found in non-lesioned area. However, inside and close to the lesions, microglial morphology changed into a more heterogeneous appearance. Here, beside tomato$^+$P2RY12$^+$ cells, we recognized tomato$^+$P2RY12^{lo} microglia in the retina or almost undetectable P2RY12 signals in tomato$^+$ cells on the RPE (Fig 8B). Notably, the protein expression pattern of TMEM119 strongly resembled P2RY12 having highly ramified tomato$^+$TMEM119$^+$ cells in unaffected regions of the retina but a decrease of TMEM119 immunoreactivity and ramification in tomato$^+$ cells close to the lesion site in the same retina and on the RPE corresponding to the lesion at CNV d7 (Fig 8C). In contrast, the increased expression of *Pcna* and *Ptma* suggested enhanced proliferation during CNV. We confirmed this by detecting EdU incorporation in tomato$^+$Iba1$^+$ rMG inside the lesion at CNV d7 (Fig 8D).

Validation of murine disease-associated expression of MHC class II in human neovascular CNV membranes

By comparing our findings in mice with the human situation, we found that *H2-Aa* expression in CNV-lesioned mice mimicks the expression in human CNV membranes of patients with neovascular AMD, both on RNA and protein level (Fig 9A–D). In humans, CNV membranes develop as newly formed fibrotic and vascularized tissue underneath the RPE and were extracted during surgery. In the murine retina, *H2-Aa* expression increased during the course of CNV development (Fig 9A). In accordance with these findings, MHC class II expression was absent in the retina distant to the lesion but could be rarely found in the center of the lesion and only very restricted to tomato$^+$ rMGs which were surrounded by MHCII$^-$ cells (Fig 9B). By contrast, the diversity increased on the RPE where we found tomato$^+$MHCII$^+$ more abundantly close to tomato$^+$MHC class II$^-$ and also tomato$^-$MHC class II$^+$ cells that could represent infiltrating cells (Fig 9B). The human CNV tissue was investigated by a novel sequencing approach specifically tailored for formalin-fixed and paraffin-embedded tissue (Boneva *et al*, 2020). The so-called Massive Analysis of cDNA ends revealed a high expression of *HLA-DR*, the human orthologous gene to the murine *H2-Aa*, specifically in the human CNV tissue but was almost absent in the controls (Schlecht *et al*, 2020). We validated this finding by staining human CNV and control tissue against HLA-DR. In the control, HLA-DR was restricted to the choroid and absent in the retina but was more abundantly expressed in the CNV membrane.

Taken together on gene and protein levels, we found time-dependent progression from control to activated proliferating microglia within 3 days following CNV induction. Furthermore, within 7 days of CNV, microglia lost acute reactivity and adopted a macrophage-like transcriptional profile. Thus microglia displayed a plastic, context-dependent phenotype. Overall, our results suggest the emergence of unique rMG states especially associated with CNV pathology that are characterized by distinct signatures and contributing to defined disease conditions.

Discussion

Our study provides a high-resolution view of the transcriptional landscape of tissue macrophages across multiple compartments of the eye and their distinct developmental pathways as well as their different turnover kinetics during homeostasis. Using scRNA-Seq, we identified several subsets of myeloid cells and their transcriptional states in the cornea, ciliary body, and retina during health. Some identified clusters showed a close relationship between homeostatic cbMΦ and cMΦ, while other clusters were significantly enriched with either cbMΦ or cMΦ. By contrast, rMG were distinct

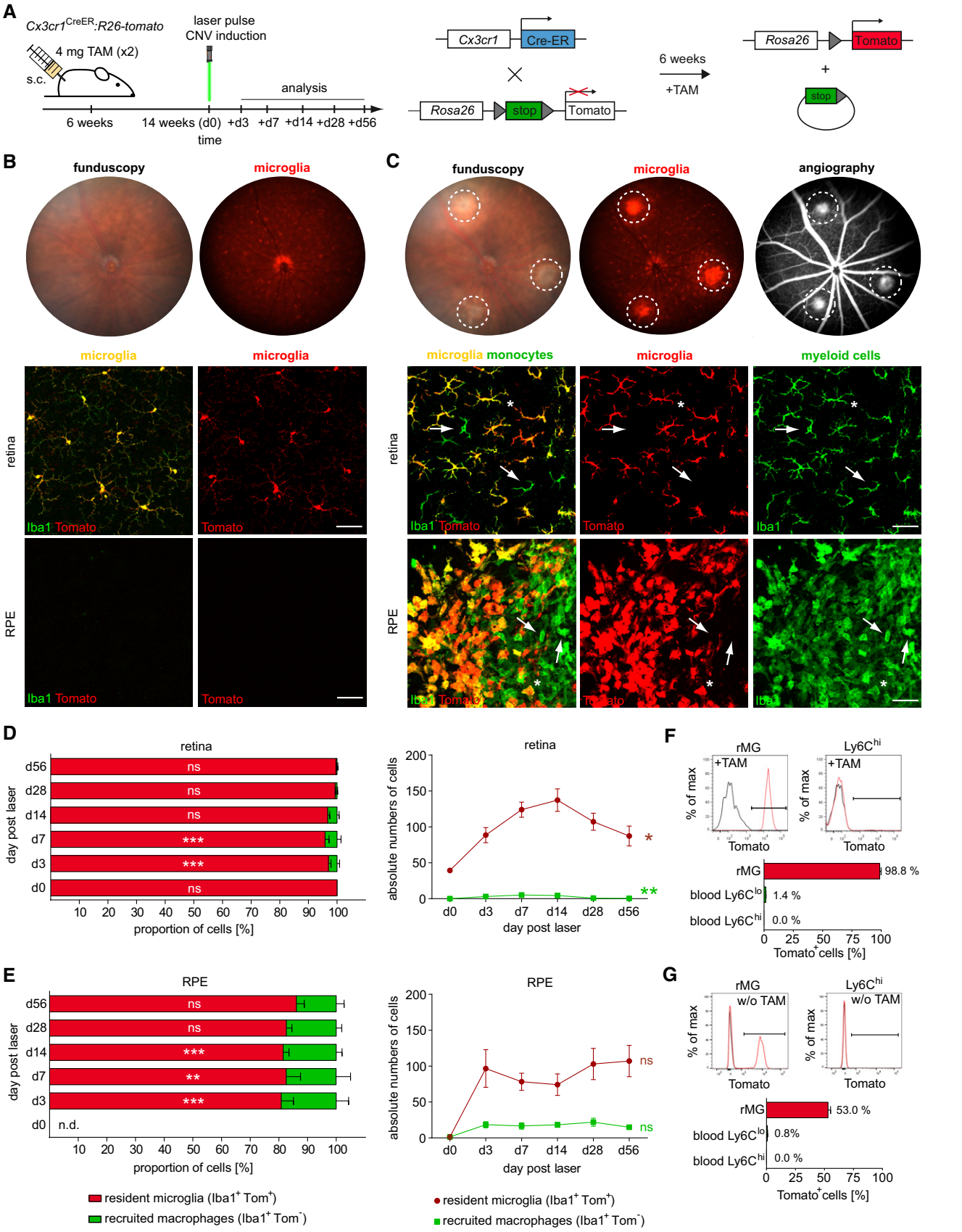
A
Cx3cr1CreER:R26-tomato
4 mg TAM (x2)
s.c.
laser pulse
CNV induction
analysis
6 weeks
14 weeks (d0)
+d3
+d7
+d14
+d28
+d56
time
Cx3cr1
Cre-ER
Rosa26
stop
Tomato
6 weeks
+TAM
B
funduscopy
microglia
C
funduscopy
microglia
angiography
microglia
microglia
microglia monocytes
microglia
myeloid cells
retina
RPE
Iba1 Tomato
Tomato
Iba1
D
retina
day post laser
d56
d28
d14
d7
d3
d0
ns
***
proportion of cells [%]
absolute numbers of cells
day post laser
E
RPE
**
n.d.
resident microglia (Iba1+ Tom+)
recruited macrophages (Iba1+ Tom-)
F
rMG
Ly6Chi
+TAM
% of max
Tomato
blood Ly6Clo
blood Ly6Chi
98.8 %
1.4 %
0.0 %
Tomato+ cells [%]
G
w/o TAM
53.0 %
0.8%

Figure 6.

Figure 6. Spatiotemporal characteristics of myeloid subsets during experimental neovascularization.

A Experimental setup. TAM was applied to 6-week-old *Cx3cr1^{CreERT2}:Rosa26-tdTomato* mice leading to the excision of the stop sequence followed by robust Tomato expression in microglia. At the age of 14 weeks (8 weeks post-TAM), three focal argon laser burns were applied to each retina to induce microglia activation and subsequent choroidal neovascularization (CNV). Analysis was performed on days (d) 3, 7, 14, 28, and 56, respectively.

B Above: Representative funduscopic pictures from living healthy *Cx3cr1^{CreERT2}:Rosa26-tdTomato* mice on d0. Funduscopy and red fluorescence visualize the fundus and regular distribution of tomato$^+$ microglia before the laser-induced lesion formation. Below: Corresponding immunofluorescence pictures. Non-lesioned retina show a regular pattern of Iba1$^+$ (green) tomato$^+$ (red) retinal microglia while macrophages are absent on the retinal pigment epithelium (RPE) under native conditions. Pictures are representative for six mice analyzed in one experiment. Scale bars represent 50 μm.

C Above: *In vivo* funduscopy on d7 post-lesion. Funduscopic and red fluorescence image depict the lesions (encircled with dashed white lines) and accumulation of tomato$^+$ microglia in *Cx3cr1^{CreERT2}:Rosa26-tdTomato* mice. Intraperitoneal fluorescein application was performed to label retinal vessels and areas of choroidal neovascularization. Below: Representative immunofluorescence for Iba1 (green) in *Cx3cr1^{CreERT2}:Rosa26-tdTomato* mice. Resident retinal microglia are Iba1$^+$tomato$^+$ (asterisks) whereas blood-derived myeloid cells are Iba1$^+$tomato$^-$ (arrows) and accumulate at sites of laser-induced CNV. Overlay is shown left. Typical pictures from six mice obtained from one independent experiment are shown. Scale bars represent 50 μm.

D Percentage (left) and absolute numbers (right) of myeloid subsets in the retina at different time points post lesion. Red columns, red lines, and red symbols represent tomato$^+$Iba1$^+$ microglia in *Cx3cr1^{CreERT2}:Rosa26-tdTomato* mice whereas green columns, green lines, and green symbols represent blood-derived tomato$^-$Iba1$^+$ myeloid cells. Left, Wilcoxon test at d3 (ns $P = 0.0625$), d28 (ns, $P = 0.25$), and d56 (ns $P = 0.125$) and paired *t*-test at d7 (***$P < 0.0001$), and d14 (***$P < 0.0001$; right, absolute numbers Kruskal–Wallis test (tomato$^+$Iba1$^+$ *$P < 0.05$, tomato$^-$Iba1$^+$ **$P < 0.01$). Data represent means ± s.e.m. from at least three mice per group (two to six lesion per mouse) out of one (d0, d14, d28, d56) or two (d7, d14) independent experiments.

E Distribution (left) and absolute numbers (right) of myeloid cells in the RPE at different time points following laser-induced lesion. Red columns, red lines, and red symbols represent tomato$^+$Iba1$^+$ microglia in *Cx3cr1^{CreERT2}:Rosa26-tdTomato* mice. Green columns, green lines, and green symbols represent blood-derived tomato$^-$Iba1$^+$ myeloid cells. Left, paired *t*-test at d3, d7, d14 (**$P < 0.01$, ***$P < 0.001$), Wilcoxon test at d28 and d56 (ns $P > 0.05$); right, absolute numbers Kruskal–Wallis test (ns $P > 0.05$). Data represent means ± s.e.m. from at least three mice per group (two to six lesion per mouse) out of one (d0, d14, d28, d56) or two (d7, d14) independent experiments.

F, G Flow cytometric measurement of tomato expression in 14-week-old *Cx3cr1^{CreERT2}:Rosa26-tdTomato* mice 8 weeks after TAM treatment (F) or with no treatment (G). Red lines represent the tomato signal and black lines the corresponding CreER-negative control. Data are presented as mean ± s.e.m. from four mice analyzed in one experiment.

from both and transcriptionally different from myeloid cells found in the steady-state cornea and ciliary body. By comparing all macrophages from the eye with the brain, rMG showed a close relationship to microglia from the brain. Certain cluster were composed of cells of all compartments, namely brain, retina, cornea, and ciliary body underlining their close relationship. Notably, short-lived cMΦ exhibited a molecular signature that was similar to BM-derived monocytes and substantially different from rMG and bMG. In a previous study, it was suggested to differentiate short- from long-lived macrophages based on their differential clustering due to differences in the expression of MHCII and CD11c (O'Koren *et al*, 2019). CMΦ were not further investigated in this study (O'Koren *et al*, 2019). In our study, we detected cMΦ and few rMG to express CD11c on protein level despite their long-lived nature but no MHC class II protein which is in line with previous reports (Hamrah *et al*, 2003; Dando *et al*, 2016). Nevertheless, our findings revealed that rMG and cbMΦ were transcriptionally unrelated to circulating myeloid cells representing a new advancement in the field. In the past, blood monocytes were thought to contribute to all of the three investigated macrophage populations in the eye (Xu *et al*, 2007; Kezic *et al*, 2008; Chinnery *et al*, 2008). These conclusions were drawn based on results of irradiation studies, but this is known today to compromise natural barriers when head shielding is not applied.

The origin of tissue macrophages in different organs could be traced back to erythromyeloid precursors in the yolk sac but the origin of macrophages in the different compartments of the eye remained unclear for a long time (Kierdorf *et al*, 2013a; Goldmann *et al*, 2016; Hagemeyer *et al*, 2016; Ensan *et al*, 2016). Therefore, we applied a conditional embryonic fate mapping model that allowed us to follow yolk sac-derived macrophages in *Cx3cr1^{CreERT2}:Rosa26-YFP* mice until birth. Our results clearly showed a contribution of embryonic precursors to rMG, cbMΦ, and cMΦ which was so far only shown before for rMG (O'Koren *et al*, 2019). Of note, the labeling efficiency in embryonic pulse labeling approaches is consistently lower than conditional fate mapping in adult mice due to the narrow time frame of developmental stages in the embryo (Ginhoux *et al*, 2010; Perdiguero *et al*, 2014; Wieghofer & Prinz, 2015; Goldmann *et al*, 2016; O'Koren *et al*, 2019). The relatively low amount of prenatal labeling of cMΦ together with their transcriptional profile resembling peripheral blood monocytes raised the question about a possible steady turnover of these cells. Consequently, we used adult *Cx3cr1^{CreERT2}:Rosa26-YFP* mice to follow the turnover of rMG, cbMΦ, and cMΦ for up to 24 weeks after YFP induction. Beside the fact that rMG and cbMΦ remained stable over time as shown before (O'Koren *et al*, 2019), cMΦ were the only cell type that showed a steady and significant decrease of YFP-expressing cells indicating a continuous replenishment. To further validate our findings, we applied other models to exclusively target bone marrow-derived peripheral blood leukocytes by parabiosis and additionally used *Flt3^{Cre}:Rosa26-YFP* mice to broadly label myeloid cells of the definitive hematopoiesis (Boyer *et al*, 2011). Again, cMΦ showed ongoing replenishment during adulthood, revealed by the temporal increase of genetically labeled partner-derived cells in wild-type parabionts and the highest contribution of *Flt3*-dependent cells to this population. Of note, our results obtained with parabiotic mice confirmed that cMΦ can derive from circulating blood cells during adulthood, but do not necessarily exclude a fetal liver origin.

In several CNS diseases, an infiltration of blood-derived monocytes is occurring (Ajami *et al*, 2011; Ma *et al*, 2017; Ajami *et al*, 2018; Jordão *et al*, 2019). To distinguish rMG (tomato$^+$) from infiltrating monocytes (tomato$^-$) during pathology, we used *Cx3cr1^{CreERT2}:Rosa26-tdTomato* mice and investigated CNV that mimics many aspects of neovascular AMD in humans. In this model, lesions are formed in the choroid affecting the overlaid retinal pigment epithelium (RPE) and the retina. Here, we found that rMG constitute a major cell population in the diseased retina and

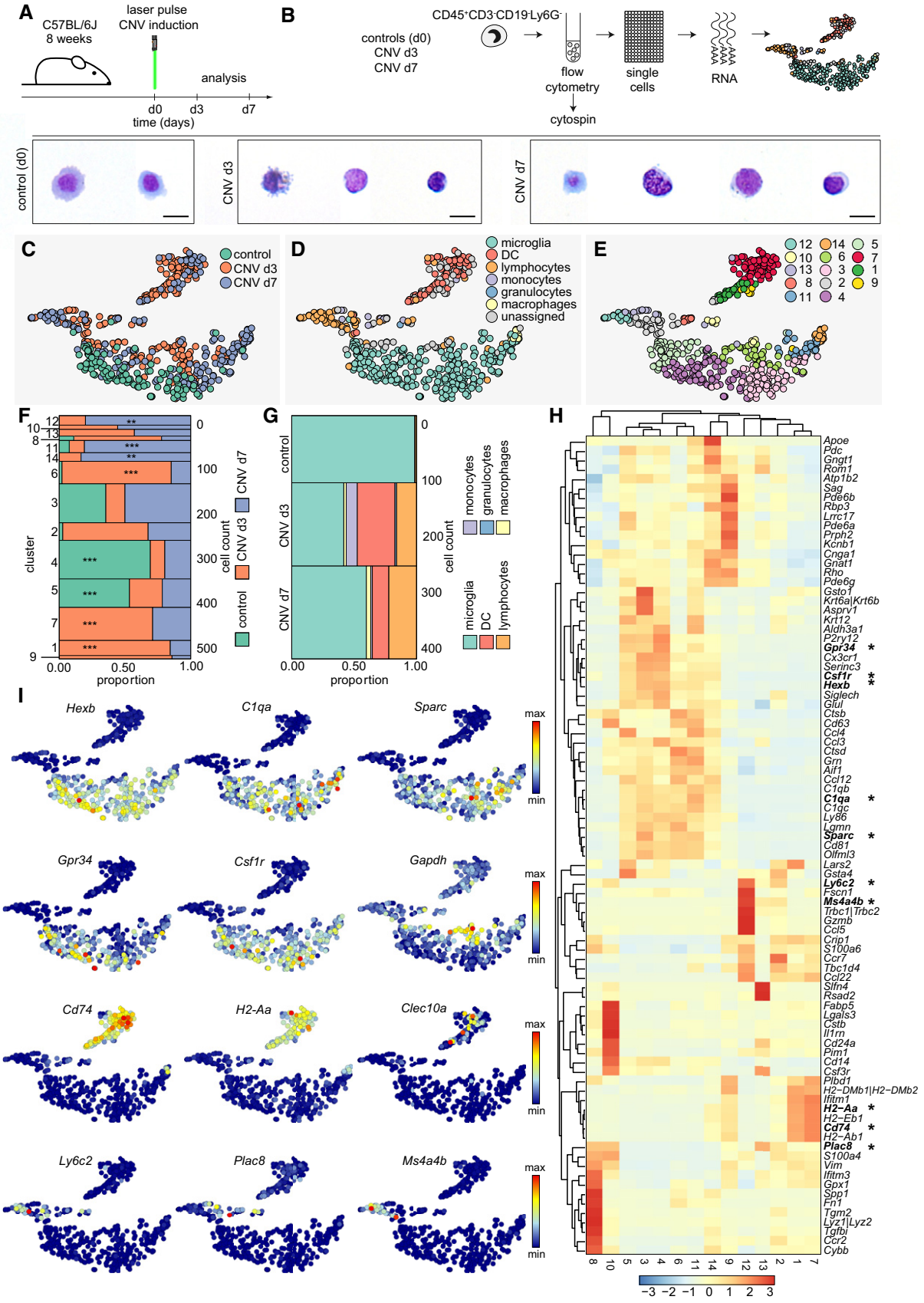
A
C57BL/6J
8 weeks
laser pulse
CNV induction
analysis
d0
d3
d7
time (days)
B
controls (d0)
CNV d3
CNV d7
CD45+CD3-CD19-Ly6G-
flow
cytometry
cytospin
single
cells
RNA
control (d0)
CNV d3
CNV d7
C
control
CNV d3
CNV d7
D
microglia
DC
lymphocytes
monocytes
granulocytes
macrophages
unassigned
E
F
cluster
cell count
proportion
G
control
CNV d3
CNV d7
monocytes
granulocytes
macrophages
microglia
DC
lymphocytes
H
Apoe
Pdc
Gngt1
Rom1
Atp1b2
Sag
Pde6b
Rbp3
Lrrc17
Pde6a
Prph2
Kcnb1
Cnga1
Gnat1
Rho
Pde6g
Gsto1
Krt6a|Krt6b
Asprv1
Krt12
Aldh3a1
P2ry12
Gpr34
Cx3cr1
Serinc3
Csf1r
Hexb
Siglech
Glul
Ctsb
Cd63
Ccl4
Ccl3
Ctsd
Grn
Aif1
Ccl12
C1qb
C1qa
C1qc
Ly86
Lgmn
Sparc
Cd81
Olfml3
Lars2
Gsta4
Ly6c2
Fscn1
Ms4a4b
Trbc1|Trbc2
Gzmb
Ccl5
Crip1
S100a6
Ccr7
Tbc1d4
Ccl22
Slfn4
Rsad2
Fabp5
Lgals3
Cstb
Il1rn
Cd24a
Pim1
Cd14
Csf3r
Plbd1
H2-DMb1|H2-DMb2
Ifitm1
H2-Aa
H2-Eb1
Cd74
H2-Ab1
Plac8
S100a4
Vim
Ifitm3
Gpx1
Spp1
Fn1
Tgm2
Lyz1|Lyz2
Tgfbi
Ccr2
Cybb
I
Hexb
C1qa
Sparc
Gpr34
Csf1r
Gapdh
Cd74
H2-Aa
Clec10a
Ly6c2
Plac8
Ms4a4b
max
min

Figure 7.

Figure 7. Detection of disease-associated myeloid cell clusters.

A Schematic diagram depicting the experimental setup.

B Isolation of single myeloid cells from the retina under healthy conditions (d0) and three (d3) or 7 days (d7) after laser pulse for unbiased sampling and single-cell RNA-seq (scRNA-seq). Increased cellular heterogeneity in lesioned mice compared with healthy controls (d0), shown by May-Grünwald-Giemsa stained cytospins. Scale bars represents 10 μm.

C *t*-SNE representation of individual cells from all conditions analyzed (control represents homeostatic microglial cells), CNV d3, CNV d7, with scRNA-seq. Each dot represents an individual cell. Color code indicates the different experimental conditions.

D *t*-SNE plot depicting different cell types.

E Unbiased cluster analysis of hematopoietic cell subpopulations found at different conditions.

F Marimekko chart showing the clusterwise distribution of 511 cells color-coded for the experimental conditions (control 122 cells, CNV d3 209 cells, CNV d7 180 cells). Hypergeometric testing revealed significantly enriched clusters for the different conditions (control: cluster 4 and 5; CNV d3: cluster 1, 6 and 7; CNV d7: cluster 11, 12, and 14), indicated by asterisks (*$P < 0.05$, **$P < 0.01$, ***$P < 0.001$).

G Marimekko chart presenting the proportion of cell types among all assigned cells (see Fig 5D) during different experimental conditions demonstrating almost pure microglia populations present at d0, whereas clusters of dendritic cells (DC), lymphocytes, monocytes, granulocytes, and macrophages are present at d3 and d7 of CNV.

H Heatmap of the 30 most regulated genes per cluster (adjusted *P*-value < 0.05 based on the negative binomial distribution). Asterisks highlight genes presented in *t*-SNE plots shown in (I).The scale bar represents the color-coded z-scores.

I Selection of *t*-SNE plots representative for different cell subsets using *Hexb*, *C1qa*, and *Sparc* to show differential expression of these genes between microglia subpopulations; *Grp34, Csf1r,* and *Gapdh* to depict cluster 6 as the highest activated microglia cluster; *Cd74, H2-Aa,* and *Clec10a* to present dendritic cell cluster; *Ly6c2, Plac8,* and *Ms4a4b* to illustrate blood-derived cell cluster.

RPE with lower numbers of recruited monocytes. This finding is in line with another model mimicking the advanced atrophic variant of AMD by pharmacologically induced injury of the RPE and subsequent photoreceptor damage. Here, endogenous rMG were the most abundant cell type in comparison with exogenously derived infiltrating monocytes (Ma *et al*, 2017).

Our single-cell profiling data provided further compelling evidence that rMG responses to pathology are quite complex and characterized by several disease-associated clusters of rMG. We further identified a broad spectrum of non-rMG cell types that are involved mainly consisting of DCs, lymphocytes, monocytes, and macrophages. To gain more insight into the temporal gene signature changes across the myeloid cells, we performed a trajectory analysis. Here, the highest diversity of cells was found at CNV d3, the time point that clearly separated from the controls and CNV d7 in the minimum spanning tree of the trajectory analysis. Nevertheless, we found that disease model-associated rMG clusters greatly differ from the rMG states found under homeostatic conditions. The molecular signatures of the rMG clusters that appeared during CNV were characterized by a down-regulation of homeostatic genes, such as *P2ry12* and *Tmem119* which we could confirm on protein level. In addition to other homeostatic microglia signature genes that were dysregulated, like *Siglech, Csf1r,* or *C1qa*, it is interesting to note that these were also down-regulated in models of photoreceptor degeneration (O'Koren *et al*, 2019). At the same time, other transcripts including *Ptma* and *Pcna* that are associated with proliferation were increased. This is in line with EdU incorporation in tomato$^+$ rMG at CNV d7. In both, the CNV model and under photoreceptor degeneration *Spp1* and *Lgals3* were up-regulated at later stages of the respective model. Finally, we were able to correlate our findings in mice with the human situation. Here, we confirmed that the increased expression of the murine *H2-Aa* (MHC class II) in the experimental CNV model is mirrored by the expression of the human counterpart *HLA-DRA* that was increased in surgically extracted CNV membranes, both on gene and protein level.

In conclusion, we identified several subsets of myeloid cells and their transcriptional states in the cornea, ciliary body, and retina during health by single-cell profiling. CbMΦ, cMΦ, and rMG all showed a contribution from prenatal sources of primitive hematopoiesis but different dependences on bone marrow-derived cells after birth leading to compartment-specific turnover rates of eye macrophages. Our results will provide new insights into the biology of myeloid subsets in the healthy and diseased eye that might open new opportunities for the treatment of ophthalmological diseases like AMD.

Figure 8. Disease stage-dependent gene expression pattern in myeloid cells during experimental CNV.

A Trajectory analysis reveals alterations in gene expression pattern over time and disease state (d0, d3, d7). Above: Trajectory heatmap depicting loss of homeostatic microglial gene expression signatures (*P2ry12, Tmem119, Csf1r, SiglecH*) and induction of genes involved in cytoskeleton modifications (*Actb*, *Tuba1c*), cell cycle progression (*Cdk1*, *Ptma*), and antigen presentation (*Cd74, H2-Aa*). Highlighted molecules (asterisks) were confirmed by immunohistochemistry shown in (B–D). Below: Trajectory plot showing the trajectory followed by myeloid cells upon CNV progress.

B Above: *P2ry12* expression is shown by trajectory analysis and represented in a *t*-SNE plot. Expression is high in homeostatic microglia (see Figs 1G and H and 7H). Below: Typical immunohistochemistry for P2RY12 (green) in unlesioned and lesioned areas. Arrows indicate lost P2RY12 expression. Asterisks mark microglial cells that maintained P2RY12 expression. Iba1 immunohistochemistry (red) to show microglia. Pictures are representative of two mice. Scale bars represent 25 μm.

C Above: *Tmem119* expression visualized by trajectory analysis and represented in a *t*-SNE plot. High signals in homeostatic microglia (see Fig 1G and H). Below: TMEM119 immunofluorescence (green) by Iba1$^+$ (red) microglia inside lesioned and non-lesioned areas in the retina and RPE. Arrows indicate microglia with lost TMEM119 expression whereas asterisks mark microglial cells that maintained TMEM119 expression. Picture is representative of two mice. Scale bars represent 25 μm.

D Above: *Ptma* expression presented by a *t*-SNE plot and its trajectory analysis over the disease course. *Ptma* expression correlates with proliferation of rMGs at d7 during CNV in *Cx3cr1*^{CreERT2}*:Rosa26-tdTomato* mice. Below: Representative immunofluorescence of proliferating EdU$^+$ (white) Iba1$^+$ (red, Tomato) microglia at sites of CNV on d7 (arrow) next to an EdU$^-$Tomato$^+$Iba1$^-$ cell (asterisks) after EdU treatment from d0 to d6. Arrowhead points toward an intravascular myeloid EdU$^-$Tomato$^-$Iba1$^+$ cell. Typical pictures from three mice obtained from one independent experiment are shown. Scale bar represents 25 μm.

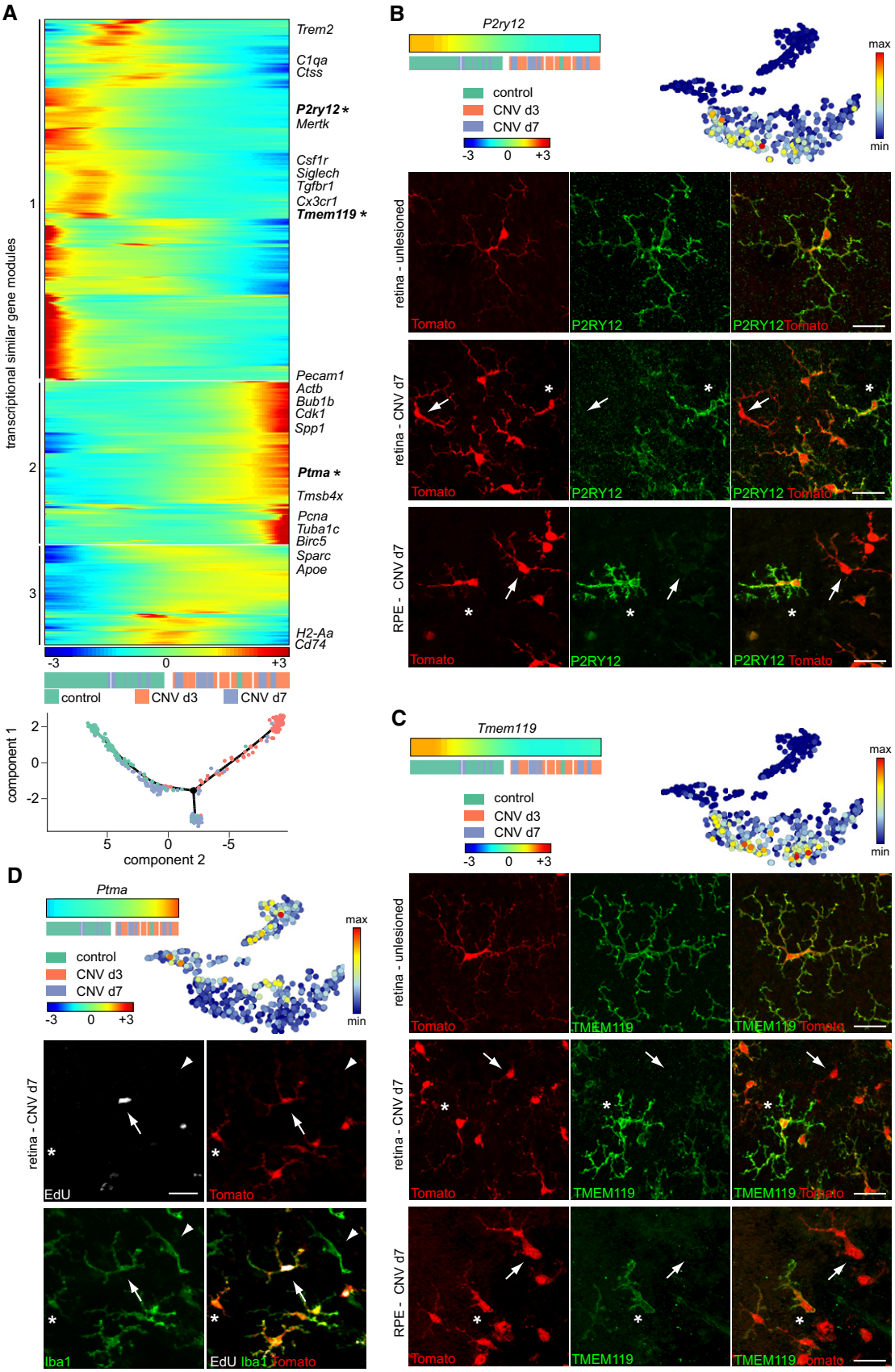
A
Trem2
C1qa
Ctss
P2ry12 *
Mertk
Csf1r
Siglech
Tgfbr1
Cx3cr1
Tmem119 *
Pecam1
Actb
Bub1b
Cdk1
Spp1
Ptma *
Tmsb4x
Pcna
Tuba1c
Birc5
Sparc
Apoe
H2-Aa
Cd74
transcriptional similar gene modules
1
2
3
-3 0 +3
control
CNV d3
CNV d7
component 1
component 2
B
P2ry12
max
min
retina - unlesioned
retina - CNV d7
RPE - CNV d7
Tomato
P2RY12
P2RY12 Tomato
C
Tmem119
TMEM119
TMEM119 Tomato
D
Ptma
EdU
Iba1
EdU Iba1 Tomato

Figure 8.

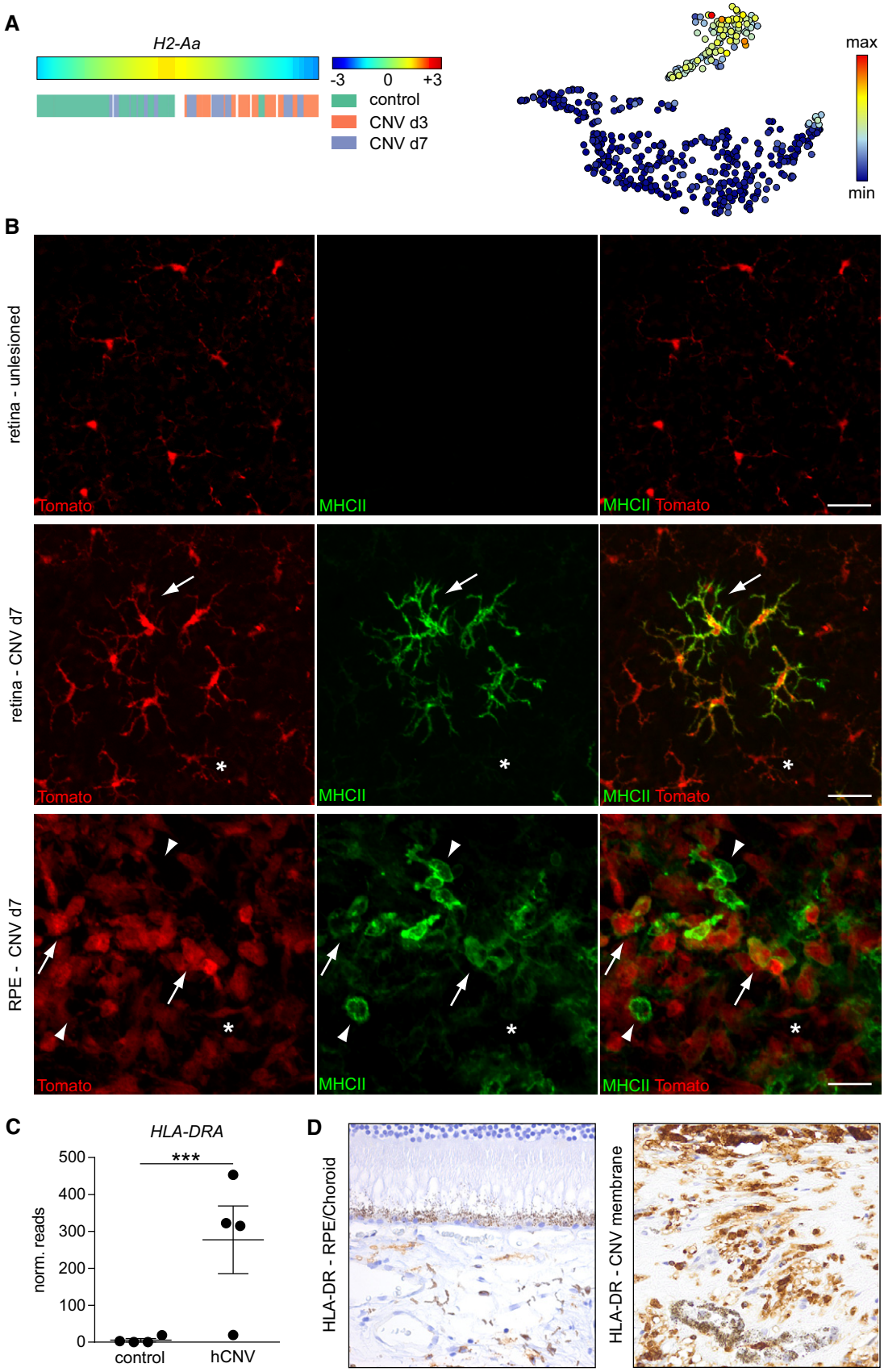

Figure 9.

Figure 9. Correlative analysis between murine experimental and human neovascular CNV.

A *H2-Aa* expression visualized by trajectory analysis and represented in a *t*-SNE plot.

B *H2-Aa* immunohistochemistry (green) by Iba1^{+} (red) microglia inside lesioned and non-lesioned areas in the retina and RPE. Arrows indicate microglia with acquired MHCII expression whereas asterisks mark microglial cells that remained MHCII negative. Picture is representative of two mice. In the RPE, arrow heads label Tom^{-}MHCII^{+} cells. Scale bars represent 25 μm.

C *HLA-DRA* mRNA expression examined by RNA-Seq via Massive analysis of cDNA ends (MACE) analysis of human formalin-fixed and paraffin-embedded (FFPE) membranes of choroidal neovascularization (CNV). Bars represent means ± s.e.m. of four investigated human samples of age-related macular degeneration associated with choroidal neovascularization and four control tissues consisting of choroid and RPE. Level of significance was calculated using DESeq ($P = 3.61 \times 10^{-21}$).

D Immunohistochemistry for HLA-DR in the RPE/choroid of one control and the CNV membrane of one patient suffering from age-related macular degeneration associated with choroidal neovascularization.

Materials and Methods

Reagents and Tools table

Reagent/Resource	Reference or Source	Identifier or Catalog Number
Acta1$^{GFP/+}$	CMV–β-actin hybrid promoter, Ajami *et al* 2007	
Ccr2RFP/+	B6.129(Cg)-*Ccr2*$^{tm2.1Ifc}$/J (Stock No: 017586, JAX mice)	
Cx3cr1GFP/+	B6.129P2(Cg)-*Cx3cr1*^{tm1Litt}/J (Stock No: 005582)	
Cx3cr1CreERT2	B6.129P2(C)-*Cx3cr1*$^{tm2.1(cre/ERT2)Jung}$/J (Stock No: 020940)	
Flt3-Cre	Benz *et al* 2008	
HexbtdT/tdT	Masuda *et al* 2020	
Itgax-DTR/EGFP	B6.FVB-*1700016L21Rik*$^{Tg(Itgax-DTR/EGFP)57Lan}$/J (Stock No. 004509, JAX mice)	
Rosa26-fl-stop-fl-tdTomato	B6.Cg-*Gt(ROSA)26Sor*$^{tm9(CAG-tdTomato)Hze}$/J (Stock No: 007909, JAX mice)	
Rosa26-fl-stop-fl-EYFP	B6.129X1-*Gt(ROSA)26Sor*$^{tm1(EYFP)Cos}$/J (Stock No: 006148, JAX mice)	
Antibodies		
rabbit anti-Iba-1, polyclonal, 1:500 (cryo) or 1:1000 (flat-mount)	WAKO, Osaka, Japan	cat # 019-19741
rabbit anti-Iba-1, polyclonal, 1:500 (cryo) or 1:1000 (flat-mount)	Synaptic Systems, Göttingen, Germany	cat # 234 013
rabbit anti-P2RY12, polyclonal, 1:500	AnaSpec, Fremont, USA	cat # AS-55043A
rabbit anti-Tmem119, polyclonal, 1:500	Synaptic Systems, Göttingen, Germany	cat # 400 002
rat anti-MHC class II (clone M5.114.15.2), monoclonal, 1:500	BioLegend, USA	cat # 107602
goat anti-GFP, polyclonal, 1:1000	Rockland Immunochemicals Inc., Gilbertsville, USA	cat # 600-106-215
goat anti-GFP, polyclonal, 1:1000	Acris Antibodies Inc., San Diego, USA	cat # R1091P
rat anti-CD74-Alexa Flour® 647 (clone In1/CD74), monoclonal, 1:100	BioLegend, USA	cat # 151003
rat anti-CD206-Alexa Flour® 647 (clone MR5D3), monoclonal, 1:100	Bio-Rad Laboratories, UK	cat # MCA2235A647
rat anti-F4/80 (clone BM8), monoclonal, 1:100	Abcam plc., UK	cat# ab16911
donkey anti-rabbit, Alexa Fluor 568®, polyclonal, 1:500	Thermo Fisher Scientific Inc., USA	cat # A10042
donkey anti-goat Alexa Fluor 647®, polyclonal, 1:500	Thermo Fisher Scientific Inc., USA	cat # A-21447
goat anti-rabbit, Alexa Fluor 647®, polyclonal, 1:500	Thermo Fisher Scientific Inc., USA	cat # A-21244
goat anti-rat, Alexa Fluor 568®, polyclonal, 1:500	Thermo Fisher Scientific Inc., USA	cat # A-11077
goat anti-rat, Alexa Fluor 647®, polyclonal, 1:500	Thermo Fisher Scientific Inc., USA	cat # A-21247
mouse anti-HLA-DP, DQ, DR, (clone CR3/43), monoclonal, 1:200	Agilent Dako, Santa Clara, CA, USA)	cat # M0775
Fc receptor blocking antibody CD16/CD32 (clone 2.4G2)	BD Pharmingen, BD Biosciences, Heidelberg, Germany	cat # 553141
rat anti-CD11b-BV421 (clone M1/70), monoclonal, 1:100	BioLegend, USA	cat # 101235
rat anti-CD45-APC-e780 (clone 30-F11), monoclonal, 1:100	Thermo Fisher Scientific Inc., USA	cat # 47-0451-82
rat anti-CD115-PE-Cy7 (AFS98), monoclonal, 1:100	Thermo Fisher Scientific Inc., USA	cat # 25-1152-82

Reagents and Tools table (continued)

Reagent/Resource	Reference or Source	Identifier or Catalog Number
rat anti-F4/80-PE-Cy7 (BM8), monoclonal, 1:100	Thermo Fisher Scientific Inc., USA	cat # 25-4801-82
mouse anti-CD64-Alexa647 (clone, X54-5/7.1), monoclonal, 1:100	BioLegend, USA	cat # 139322
rat anti-Ly6C-FITC (clone AL-21), monoclonal, 1:100	BD Pharmingen, BD Biosciences, Heidelberg, Germany	cat # 553104
rat anti-Ly6G-PE-Cy7 (clone 1A8), monoclonal, 1:100	BD Pharmingen, BD Biosciences, Heidelberg, Germany	cat # 560601
anti-CD45-BV421 (clone 30-F11), monoclonal, 1:100	BioLegend, USA	cat # 103134
rat anti-CD3-PE-Cy7 (clone 17A2), monoclonal, 1:100	BioLegend, USA	cat # 100220
rat anti-CD19-PE-Cy7 (clone 6D5), monoclonal, 1:100	BioLegend, USA	cat # 115519
Oligonucleotides and other sequence-based reagents		
RNAprotect Tissue Reagent	QIAGEN, Hilden, Germany	cat # 76104
RNeasy Plus Micro Kit	QIAGEN, Hilden, Germany	cat # 74034
Buffer RLT Plus	QIAGEN, Hilden, Germany	cat # 1053393
SMARTer Ultra Low Input RNA Kit for Sequencing v4	Clontech Laboratories, Inc., Mountain View, CA, USA	cat # 634456
KAPA SYBR FAST ABI Prism Library Quantification Kit	Roche, Basel, Switzerland	cat # KK4835
Illumina TruSeq SR Cluster Kit v3	Illumina, USA	cat # GD-401-3001
TruSeq SBS v3 Reagents	Illumina, USA	cat # FC-401-3001
AMPure/RNAClean XP beads	Beckman Coulter, München, Germany	cat # A63987
Quick-RNA FFPE Kit	Zymo Research, USA	cat # R1008
DNAse I digestion using the Baseline-ZERO kit	Lucigen Corporation, USA	cat # DB0715K
Qubit RNA HS Assay Kit	Thermo Fisher Scientific Inc., USA	cat # Q32852
RNA Pico Sensitivity Assay	Perkin Elmer, USA	cat # CLS960012
Chemicals, enzymes and other reagents		
Fluorescein	Alcon Pharma GmbH	cat # H12588-0113
Tissue-Tek® O.C.T.TM Compound	Sakura Finetek Germany GmbH	cat # 4583
in Vitro-Clud® (R. Langenbrinck GmbH, Emmendingen, Germany).	R. Langenbrinck GmbH, Emmendingen, Germany	cat # 04-0001
May-Grünwald (Merck 101424)	Merck	cat # 101424
Giemsa (Merck 109204)	Merck	cat # 109204
Tamoxifen (TAM, T5648-1G, Sigma-Aldrich, Taufkirchen, Germany)	Sigma-Aldrich, Taufkirchen, Germany	cat # T5648-1G
corn oil (Sigma-Aldrich, C8267-500ml)	Sigma-Aldrich, Taufkirchen, Germany	cat # C8267-500ml
Hank's Balanced Salt Solution	Thermo Fisher Scientific Inc., USA	cat # 14170138
eBioscience™ Fixable Viability Dye eFluor™ 506	Thermo Fisher Scientific Inc., USA	cat # 65-0866-14
eBioscience™ Fixable Viability Dye eFluor™ 780	Thermo Fisher Scientific Inc., USA	cat # 65-0865-18
Software		
FACSDiva software	BD Biosciences, Heidelberg, Germany	
FlowJo software (7.6.1)	Treestar (BD Biosciences, Heidelberg, Germany)	
IMARIS 8.0	Bitplane, Switzerland	
FV10-ASW 4.2 Viewer	Olympus, Tokyo, Japan	
GraphPad Prism (Version 6.0)	GraphPad Software, USA	
Other		
RS 2000 Biologica x-Ray irradiator	Rad Source Technologies, USA	
VISULAS 532s	Carl Zeiss Meditec AG, Jena, Deutschland	
Olympus BX-61 fluorescence microscope	Olympus, Tokyo, Japan	
Olympus DP71 color camera	Olympus, Tokyo, Japan	
BZ-9000 fluorescence microscope	Keyence, Osaka, Japan	
Fluoview FV 1000 confocal microscope	Olympus, Tokyo, Japan	
20x 0.95 NA XLUMPlanFL N objective	Olympus, Tokyo, Japan	

Reagents and Tools table (continued)

Reagent/Resource	Reference or Source	Identifier or Catalog Number
20x 0.75 NA U Plan S Apo objective	Olympus, Tokyo, Japan	
40x 0.95 NA U Plan S Apo objective	Olympus, Tokyo, Japan	
DMi-8 confocal microscope	Leica, Wetzlar, Germany	
20x NA 0.75 CS2 objective	Leica, Wetzlar, Germany	
FACSCanto II	BD Biosciences, Heidelberg, Germany	
FACSAria III	BD Biosciences, Heidelberg, Germany	
MoFlo High Speed Cell Sorter	Beckman Coulter, München, Germany	
HiSeq 3000	Illumina, USA	
HiSeq 1000	Illumina, USA	
NextSeq 500	Illumina, USA	
mosquito® HTS Nanolitre Liquid Handler	SPT Labtech, USA	
Autostainer	Agilent Dako, Santa Clara, CA, USA	
Qubit Fluorometer	Life Technologies, USA	
LabChip GXII Touch	Perkin Elmer, USA	
384-well plates	Biorad, Munich, Germany	
RNeasy Plus Micro Kit	QIAGEN, Hilden, Germany	cat # 74034
Click-iT® EdU Alexa Fluor® 488 Imaging Kit	Thermo Fisher Scientific	cat # C10337
Dako REALTM EnVisionTM Detection System Kit	Agilent Dako, Santa Clara, CA, USA	cat # K406511-2

Methods and Protocols

Mice

In this study, C57BL/6J mice were used as wild-type (WT) mice. All transgenic lines (*Acta1*$^{GFP/+}$, *Ccr2*$^{RFP/+}$, *Cx3cr1*$^{GFP/+}$, *Hexb*$^{tdT/tdT}$, *Cx3cr1*^{CreERT2}, *Flt3*^{Cre}, *Rosa26-fl-stop-fl*-EYFP (*Rosa26-YFP*), and *Rosa26-fl-stop-fl-tdTomato* (*Rosa26-tdTomato*)) were bred on a C57BL/6J background under specific pathogen-free conditions and devoid of *Crb1* (*RD8*) mutations. *Itgax*-DTR/EGFP (CD11c-GFP) mice were purchased from Jackson Laboratory (Stock No. 004509, C57BL/6J background). *Cx3cr1*^{CreERT2} were crossed to *Rosa26-YFP* or *Rosa26-tdTomato*. *Flt3*^{Cre} were crossed to *Rosa26-YFP*. All animal experiments were approved by local administration and were performed in accordance with the respective national, federal, and institutional regulations.

Tamoxifen treatment

For induction of the nuclear CreER-T2 recombinase activity in adult animals, 6- to 8-week-old *Cx3cr1*^{CreERT2} mice of mixed gender were treated with 4 mg Tamoxifen (TAM, T5648-1G, Sigma-Aldrich, Taufkirchen, Germany) dissolved in 200 µl corn oil (Sigma-Aldrich, C8267-500ml) and injected subcutaneously at two time points 48 h apart. For pulse labeling experiments, the CreER-T2 recombinase activity was induced in *Cx3cr1*^{CreERT2}:*Rosa26-YFP* embryos with 200 µl of 20 mg/ml TAM and 10 mg/ml Progesterone dissolved in corn oil by i.p. injections into pregnant females at 9 days post-coitum.

BM transplantation

Eight-week-old recipient wild-type mice were irradiated and reconstituted with 5×10^6 bone marrow cells derived from femur and tibia of an adult donor (*Acta1*$^{GFP/+}$) mice, injected into the tail vein of recipients. Mice received whole-body irradiation (11 Gy) 24 h prior to bone marrow reconstitution with an RS 2000 Biologica x-Ray irradiator. After 4 weeks, reconstitution efficiency in the blood was assessed by flow cytometry and found to be > 90% in Ly6C^{hi} monocytes.

Parabiosis

Pairs of female WT and *Acta1*$^{GFP/+}$ mice were surgically connected for 2, 12, and 20 weeks as previously described (Ajami *et al*, 2007). Blood sharing was verified between 10 and 15 days after surgery and at the day of dissection by flow cytometry (see below). After transcardial perfusion with PBS, eyes were fixed in 4% paraformaldehyde (PFA, wt/vol) for 1 h at RT and flat-mounted after free-floating immunofluorescence staining of the retina (see below).

Laser-induced choroidal neovascularization model

Mice of mixed gender that underwent induction of choroidal neovascularization (Tobe *et al*, 1998) were anesthetized with a mixture of ketamine (100 mg/kg) and xylazine (6 mg/kg), and pupils were dilated with a combination of 0.5% tropicamide and neosynephrine-POS 5%. Corneal gel was applied to maintain hydration of the cornea and reduce media opacifications. Mice were placed in front of an argon laser (VISULAS 532s, ZEISS) after the pupils were completely dilated. A cover slip with a drop of gel was placed on the eye as a contact lens to convert the curved cornea surface to a planar surface. Three laser burns at equal distance from the optic disk were induced by an Argon laser with a wavelength of 532 nm, a power of 150 mW, a fixed diameter of 100 µm, and duration of 100 ms. Only burns that produced a bubble as a sign for retinal pigment epithelial rupture were included in the study. After laser treatment, mice were

then placed on a pre-warmed warming plate at 35°C until they recovered from anesthesia. Fundus imaging and fluorescence angiography was performed by injecting 40 µl Fluorescein (ALCON 10%, H12588-0113) diluted 1:20 with 0.9% NaCl per 20 g mouse. At the respective days after laser treatment (d3, d7), mice were transcardially perfused with PBS, eyes were fixed in 4% paraformaldehyde (PFA, wt/vol) for 1 h at RT and flat-mounted after free-floating immunofluorescence staining of the retina (see below).

Fluorescence microscopy

After transcardial perfusion with phosphate-buffered saline (PBS), eyes were fixed in 4% PFA for 1 h at RT and processed as previously described for flat mounts (Pitulescu *et al*, 2010) or dehydrated in 30% sucrose and embedded in Tissue-Tek® O.C.T.TM Compound (Sakura Finetek Germany GmbH) for cryosections. In brief, eye cups were dehydrated in 30% sucrose after fixation and embedded in Tissue-Tek. 12 µm sections were then blocked with PBS containing 5% bovine serum albumin and permeabilized with 0.1% Triton X-100 in blocking solution. Primary antibodies were added over night at a dilution of 1:500 (cryo) or 1:1,000 (flat mount) for Iba-1 (019-19741, WAKO, Osaka, Japan; 234 013, Synaptic Systems, Göttingen, Germany), 1:500 for P2RY12 (AS-55043A, AnaSpec, Fremont, USA), Tmem119 (400 002, Synaptic Systems, Göttingen, Germany) and MHC class II (clone M5.114.15.2, 107602, BioLegend) and 1:1,000 for anti-GFP (600-106-215, Rockland Immunochemicals Inc., Gilbertsville, USA; R1091P, Acris Antibodies Inc., San Diego, USA), 1:100 for CD74-Alexa Flour® 647 (clone In1/CD74, 151003, BioLegend, USA), and CD206-Alexa Flour® 647 (clone MR5D3, MCA2235A647, Bio-Rad Laboratories, UK) at 4°C. Secondary antibodies were added in a dilution of 1:500 (Alexa Fluor® 568 and Alexa Fluor® 647, Thermo Fisher Scientific, Waltham, USA) for 2 h at RT (cryo) or overnight at 4°C (flat mount). Nuclei were counterstained with 4′,6-Diamidin-2-phenylindol (DAPI). Images were taken using a conventional fluorescence microscope (Olympus BX-61 with a color camera (Olympus DP71)) (Olympus, Tokyo, Japan) or BZ-9000 (Keyence, Osaka, Japan), and the confocal pictures were taken with a Fluoview FV 1000 (Olympus) using a 20x 0.95 NA XLUMPlanFL N, 20x 0.75 NA U Plan S Apo, or a 40x 0.95 NA U Plan S Apo or a DMi-8 (Leica) with a 20x NA 0.75 CS2 (Leica 506517).

Cytospin

After sorting of the cells for scRNA-seq, the same tube was further sorted in another tube containing 500 µl of HBSS and heat-inactivated fetal calf serum (1:1) and kept on ice until centrifugation. Samples were transferred to centrifugation tubes and centrifuged at 64 *g* for 5 min. Next samples were transferred to a specific cytochamber system (Hettich Instruments, Tuttlingen, Germany) and centrifuged for 5 min at 36 *g*; supernatant was removed followed by a drying centrifugation step (3 min, 122 *g*) and subsequent cell staining. Prior to the staining, May-Grünwald (Merck 101424) and the diluted Giemsa (Merck 109204) solutions have to be prepared freshly, filtered before use, and were applied at RT. Air-dried slide with spinned down cells underwent a 4-min incubation in May-Grünwald solution (Merck 1.01424). After that, the solution is diluted by adding an equal volume of aqua bidest for another 4 min. Next, the diluted May-Grünwald solution was discarded and the slides were rinsed with aqua bidest. The Giemsa staining has to be incubated for 15 min at a dilution of 1:10 in aqua bidest and washed off with aqua bidest before a brief incubation in 100% ethanol followed by xylol before embedding.

In vivo EdU proliferation assay

Eight weeks following TAM injection *Cx3cr1*^{CreERT2}*:Rosa26-tdTomato* mice underwent laser treatment to induce choroidal neovascularizations (d0). EdU (100 µg/day) was applied intraperitoneally from day 0 to day 6 once daily. Mice were sacrificed at day 7. EdU was visualized by the Click-iT® EdU Alexa Fluor® 488 Imaging Kit (Thermo Fisher Scientific, C10337) according to the manufacturers protocol, nuclei by DAPI and myeloid cells by anti-Iba1 and secondary anti-rabbit Alexa Fluor® 647 antibody.

Identification of microglia and circulation-derived monocytes

Cx3cr1^{CreERT2}*:Rosa26-tdTomato* mice of mixed gender were lasered 8 weeks after TAM treatment to induce choroidal neovascularization. After perfusion with PBS at the indicated time points following laser treatment, retinal and RPE/choroidal whole-mounts were fixed, stained, and flat-mounted. The lesions were imaged on a Fluoview FV1000 (see above). Iba1^{+} cells were identified in the stack volume using IMARIS and automatically classified as Iba1^{+}tom^{+} microglia or Iba1^{+}tom^{-} periphery-derived monocytes, according to the calculated stack-specific background in the tomato channel. The percentage of tomato$^{+/-}$ was determined among all Iba1^{+} cells in the whole lesioned stack volume imaged at a 20× magnification.

Flow cytometry

Eyecups were carefully dissected under a binocular to separate retina, cornea and ciliary body. Monocytes were isolated from bone marrow. Cornea and ciliary body tissues were separated into single-cell suspensions by Collagenase D digestion, resuspension, and filtration through 70 µm cell sieve. Retina was dissociated by resuspension. Two mice were pooled for ciliary body samples if not indicated differently. Dead cell exclusion was performed by incubation with fixable viability dye 506 or 780 (eBioscience), respectively. Anti-CD16/CD32 Fc block was performed to avoid unspecific binding. Cells were stained with primary antibodies directed against CD11b (M1/70), CD45 (30-F11), CD115 (AFS98), F4/80 (BM8) (eBioscience), CD64 (X54-5/7.1), Ly6C (AL-21), and Ly6G (1A8) at 4°C for 20 min at a concentration of 1:200 if not indicated differently. CD206 (C068C2) (BioLegend) was incubated at 4°C for 45 min. Cells were washed and analyzed using a FACS-Canto II or a FACSAria III (RFP detection in *Ccr2*$^{RFP/+}$ mice) (BD Biosciences, Heidelberg, Germany). Sorting was performed using a MoFlo High Speed Cell Sorter (Beckman Coulter, München). Data were acquired with FACSDiva software (Becton Dickinson). Postacquisition analysis was performed using FlowJo software. (Gating strategy: Fig EV6).

RNA sequencing and analysis

C57BL/6J mice negative for the *RD8* mutation were purchased from Charles River and analyzed at the age of 8 weeks. Total bulk RNA was extracted from directly into RNAprotect buffer (QIAGEN, Hilden, Germany) FACS-sorted CD45^{+}CD11b^{+}Ly6C^{-}Ly6G^{-} retinal and brain microglia, CD45^{+}CD11b^{+}CD64^{+}F4/80^{+}Ly6C^{-}Ly6G^{-} cornea macrophages and CD45^{+}CD11b^{+}SSc^{lo}CD115^{+}Ly6C^{hi} BM monocytes, according to the "Purification of total RNA from animal and human

cells" protocol of the RNeasy Plus Micro Kit (QIAGEN). In brief, cells were stored and shipped in RNAprotect buffer at 2–8°C. After pelleting, the RNAprotect buffer was replaced by RLT Plus buffer (QIAGEN) and the samples were homogenized by vortexing for 30 s. Genomic DNA contamination was removed using gDNA Eliminator spin columns. Next ethanol was added and the samples were applied to RNeasy MinElute spin columns followed by several wash steps. Finally, total RNA was eluted in 12 µl of nuclease free water. Purity and integrity of the RNA were assessed on the Agilent 2100 Bioanalyzer with the RNA 6000 Pico LabChip reagent set (Agilent, Palo Alto, CA, USA).

The SMARTer Ultra Low Input RNA Kit for Sequencing v4 (Clontech Laboratories, Inc., Mountain View, CA, USA) was used to generate first strand cDNA from 150 to 600 pg total RNA. Double-stranded cDNA was amplified by LD PCR (12–14 cycles) and purified via magnetic bead cleanup. Library preparation was carried out as described in the Illumina Nextera XT Sample Preparation Guide (Illumina, Inc., San Diego, CA, USA). 150 pg of input cDNA were tagmented (tagged and fragmented) by the Nextera XT transposome. The products were purified and amplified via a limited-cycle PCR program to generate multiplexed sequencing libraries. For the PCR step, 1:5 dilutions of index 1 (i7) and index 2 (i5) primers were used. The libraries were quantified using the KAPA SYBR FAST ABI Prism Library Quantification Kit (Kapa Biosystems, Inc., Woburn, MA, USA). Equimolar amounts of each library were pooled, and the pools were used for cluster generation on the cBot with the Illumina TruSeq SR Cluster Kit v3. The sequencing run was performed on a HiSeq 1000 instrument using the indexed, 50 cycles single-read (SR) protocol, and the TruSeq SBS v3 Reagents according to the Illumina HiSeq 1000 System User Guide. Image analysis and base calling resulted in .bcl files, which were converted into .fastq files with the bcl2fastq v2.18 software. RNA extraction, library preparation, and RNA-seq were performed at the Genomics Core Facility "KFB—Center of Excellence for Fluorescent Bioanalytics" (University of Regensburg, Regensburg, Germany).

Differential Gene Expression Analysis and Data Visualization: Fastq files were quality controlled using FastQC (Andrews, 2010) and FastQ Screen (Winget, 2011) software. Raw data were then mapped to the mouse genome (Gencode version M11 (Mudge & Harrow, 2015)) using the STAR 2.5.2b aligner (Dobin *et al*, 2013). Subsequently aligned reads were matched with transcriptome annotation, and gene counts were generated using featureCounts 1.5.1 (Liao *et al*, 2014). Read count normalization and differentially gene expression analysis was performed using the limma/voom pipeline (limma 3.34.0) (Law *et al*, 2014). Data visualization was performed using the gplots and ggplot2 packages in R. Spider Plots: Log2fold changes vs. brain microglia were calculated through limma/voom for retinal microglia, cornea macrophages, and bone marrow monocytes (Warnes *et al*, 2016). This three-dimensional dataset was subsequently projected into two dimensions as previously described van de Laar *et al*, 2016). Briefly x′ and y′ dimensions were calculated as $X' = \cos(0°)*X + \cos(120°)*Y + \cos(240°)*Z$ and $Y' = \sin(0°)*X + \sin(120°)*Y + \sin(240°)*Z$ with X = coMacvsbMG, Y = BM-MovsbMG, and Z = rMGvsbMG. Visualization was performed using ggplot2.

Single-cell RNA sequencing

C57BL/6J female mice devoid of the *RD8* mutation were purchased by Charles River and analyzed at the age of 8 weeks. After perfusion with PBS and careful dissection of retina, ciliary body, and cornea under a binocular, viable $CD45^+CD3^-CD19^-Ly6G^-$ cells from each compartment (retina, ciliary body and cornea) were pooled from five individual mice prior to flow cytometry-based purification into 384-well plates (Bio-Rad, Munich, Germany) (see "flow cytometry" above) in two independent experiments. The data from these mice were used as control for the CNV experiments. For CNV experiments, C57BL/6J female mice underwent laser-induced choroidal neovascularization (see above). At CNV d3 and d7, lesioned central retina from ten eyes out of seven (d3) or eight (d7) mice was cut out, processed for flow cytometry, and pooled per condition prior to purify viable $CD45^+CD3^-CD19^-Ly6G^-$ cells into 384-well plates. Five non-lesioned C57BL/6J mice served as controls. The used antibodies were CD45-BV421 (30F-11, cat# 103134), CD3-PE-Cy7 (17A2, cat# 100220), and CD19-PE-Cy7 (6D5, cat# 115519) from BioLegend and Ly6G-PE-Cy7 (1A8, cat# 560601, BD Biosciences). Before and after sorting, the 384-well plate were centrifuged for 2 min at 845 *g* 4°C. Subsequently, sorted plates were snap-frozen in liquid nitrogen and stored at −80°C until RNA extraction. Single-cell RNA sequencing was performed using CEL-Seq2 method (Hashimshony *et al*, 2016) with several modifications as previously described (Herman *et al*, 2018). A fivefold volume reduction was achieved using a nanoliter-scale pipetting robot (Mosquito HTS, TTP Labtech). 160 nl of reverse transcription reaction mix and 2.2 µl of second strand reaction mix was used to convert RNA into cDNA. cDNA were pooled before cleanup and *in vitro* transcription, generating two libraries from one 384-well plate containing the barcodes 1–192. For cleanup, AMPure/RNAClean XP beads (Beckman Coulter) were used at a beads-to-sample ratio of 0.8:1. Other steps were performed as described in the original protocol. 18 libraries (1,536 single cells) were sequenced per lane (pair-end multiplexing run, 100 bp read length) of an *Illumina HiSeq* 3000 sequencing system at a depth of ~ 130,000–200,000 reads per cell. Paired-end reads were aligned to the transcriptome using bwa (version 0.6.2-r126) with default parameters Li & Durbin, 2010). The transcriptome contained all RefSeq gene models based on the mouse ENCODE VM9 release downloaded from the UCSC genome browser comprising 57,207 isoforms with 57,114 isoforms mapping to fully annotated chromosomes (1–19, X, Y, M). All isoforms of the same gene were merged to a single gene locus and gene loci that overlap of > 75% were merged to gene groups resulting in 34,111 gene groups. The 50 bp of the right mate of each read pair were mapped to the ensemble of all genes and to 92 ERCC spike-ins in sense direction (Baker *et al*, 2005). Only uniquely mapped reads were retained. The left read contained the barcode information: the first six bases corresponded to the unique molecular identifier (UMI) followed by six bases representing the cell-specific barcode. The remainder of the left read contained a polyT stretch. The left read was omitted from quantification. For each cell barcode, the number of UMIs per transcript was counted and aggregated across all transcripts derived from the same gene locus. Based on the binomial distribution, the number of observed UMIs was converted into transcript counts (Grün *et al*, 2014). The number of quantified genes was 21,129 for laser-induced choroidal neovascularization and 21,427 genes for the comparison between macrophage populations. Identification and visualization of different subpopulations as well as differential gene expression analysis was performed with the RaceID3 algorithm version 0.1.5 (Herman *et al*, 2018). All samples were processed on the same day.

Mitochondrial genes were excluded prior to analysis. Down-scaling to 1,000 transcripts was used for data normalization, and cells with < 1,500 transcripts were discarded. Furthermore, cells expressing > 2% of Kcnq1ot1, a potential marker for low-quality cells (Grün *et al*, 2016), were excluded from analysis. RaceID3 analysis was performed with the following parameters: mintotal = 1,000, minexpr = 5, outminc = 5, FSelect = TRUE, and probthr = 10^{-8}. Differentially expressed genes were identified similar to the DESeq2 algorithm (Anders & Huber, 2010).

Clusterwise enrichment analysis of cells from the respective anatomical locations or treatments was conducted using hypergeometric testing. Here, the number of cells per cluster per condition and the total number of cells per condition were taken into account. Statistical testing was achieved using the phyper function in R for the probability to assess the probability that n or more cells from a given condition are found per cluster by chance.

Trajectory analysis to assess stepwise changes of cell states was performed using Monocle version 2.99.319. Default parameters were applied besides the following adjustments: genes expressed in $n \geq 3$ cells with a mean expression of ≥ 0.5; in the newCellDataSet function – lowerDetectionLimit = 0.5; in the detectGenes function – min_expr = 0.5; in the reduceDimensions function – max_components = 2, num_dim = 6, reduction_method="tSNE"; in the clusterCells function – num_clusters = 11; for the plot_pseudotime_heatmap function differentially expressed genes at a significance level of *P*val ≤ 0.01 were included.

Confirmatory trajectory analysis was performed using the StemID2 algorithm version 17. Clusters with $n \geq 5$ cells were included. A threshold of *P*thr = 0.01 was applied. Trajectories were analyzed as suggested by the plotgraph function with a threshold of scthr = 0.01. For the control-to-day7, trajectory clusters 5->4->3->11->14 were considered and for the control-to-day3 trajectory clusters 5->4->3->6. For pseudotemporal ordering, default parameters were used (Trapnell *et al*, 2014). Heatmaps were visualized using the pheatmap R package version 1.0.12.

Human tissue

Whole human eyes (ciliary body melanoma) or eye tissue (CNV membrane) were taken with consent with the patients during surgery at the Eye Clinic, University Medical Center Freiburg. MACE RNA Sequencing was performed on four FFPE CNV membranes that were extracted from patients with neovascular Four age-matched FFPE RPE-choroidal specimens were obtained from the macular region of enucleated eyes suffering from ciliary body melanoma served as controls. The macular RPE and choroid was unaffected in these eyes as confirmed by routine histology. FFPE tissue was sliced with 7 μm thickness and placed on glass slides. For immunohistochemistry, deparaffinization was performed (15 min xylol followed by descending ethanol concentration, 2× for 1 min for each concentration (100, 96, 70%)) and finally aqua dest at room temperature. Next, citrate buffer (pH = 6) was applied for 40 min at 95°C. The following steps were performed in an Autostainer (Agilent Dako, Santa Clara, CA, USA) with the Dako REAL™ EnVision™ Detection System Kit (K406511-2, Agilent Dako). Peroxidase blocking reagent (5 min) was rinsed with Tris buffer (0.5 M TRIS, 9% NaCl, 0.5% Tween 20). Primary antibodies (Anti-HLA-DP, DQ, DR, M0775, clone CR3/43, 1:400, Agilent Dako, Santa Clara, CA, USA) were incubated for 30 min, washed with Tris, treated with secondary antibody for 20 min, and finally visualized by diaminobenzidin according to the manufacturer's instructions for 5–10 min. After rinsing with aqua dest, nuclei were counterstained with hematoxylin–eosin for 15 s. After washing with water, the deparaffination protocol was conducted in reverse order before embedding in Vitro-Clud® (R. Langenbrinck GmbH, Emmendingen, Germany).

RNA sequencing using massive analysis of cDNA ends (MACE)

Total RNA was isolated from formalin-fixed and paraffin-embedded (FFPE) sections of all specimens using the Quick-RNA FFPE Kit (Zymo Research, USA). Following a DNAse I digestion using the Baseline-ZERO kit (Epicentre, USA), the RNA concentration was measured with the Qubit RNA HS Assay Kit on a Qubit Fluorometer (Life Technologies, USA). The RNA quality was determined with the RNA Pico Sensitivity Assay on a LabChip GXII Touch (PerkinElmer, USA). The fragment size of all RNA samples ranged between 120 and 150 bp. The preparation of massive analysis of cDNA ends (MACE) libraries was carried out using 1 μg of total RNA, as previously described (Zajac *et al*, 2015). The barcoded libraries (four CNV membranes and four control samples) were sequenced simultaneously on the NextSeq 500 (Illumina, USA) with 1 × 75 bp. Illumina sequence reads and were processed with an in-house analysis pipeline (GeneXPro, Germany), including TrueQuant PCR bias elimination and mapping against the human reference genome. For MACE analysis, normalization and test for differential gene expression were calculated using the DEGseq (Wang *et al*, 2010). Differential gene expression was quantified as the $\log_2$ ratio of the normalized values between the two libraries (CNV vs. control). The sequencing data reported in the current article have been deposited in the Gene Expression Omnibus database under the accession number GSE146887 (Schlecht *et al*, 2020).

Statistical analysis

Statistical analysis was performed using GraphPad Prism (GraphPad Software, version 6.0, La Jolla, USA). Data were tested for normality applying the Kolmogorov–Smirnov test. If normality was given, an unpaired *t*-test was applied or one-way ANOVA, if not indicated otherwise. If the data did not meet the criteria of normality, the Mann–Whitney or Kruskal–Wallis test was applied. Differences were considered significant when *P*-value < 0.05.

Data availability

The sequencing data reported in the current article have been deposited in the Gene Expression Omnibus database under the accession numbers GSE160845 (mouse bulk RNA-seq; https://www.ncbi.nlm.nih.gov/geo/query/acc.cgi?acc=GSE160845) and GSE160797 (mouse single-cell RNA-seq; https://www.ncbi.nlm.nih.gov/geo/query/acc.cgi?acc=GSE160797).

Expanded View for this article is available online.

Acknowledgements

The authors thank Marc Leinweber, Gabriele Prinz, Maria Oberle, Johannes Baumann, Katrin Seidel, Eileen Barleon, Constance Hobusch, Angela Ehrlich,

Heidrun Kuhrt, and Sylvia Zeitler for excellent technical assistance, M. Follo and team at lighthouse fluorescence technologies core Facility, University Medical Center, Freiburg for cell sorting, CEMT at University of Freiburg for excellent animal care, KFB, Center of Excellence for Fluorescent Bioanalytics, Regensburg for bulk RNA-seq analysis, Jonas Neher, Tübingen (*Ccr2-RFP*), Frédéric Geissmann, New York for providing *Flt3*^{Cre}*:Rosa26-YFP* mice. Special thanks to Sagar and Dominic Grün, MPI-IE, Freiburg, for providing excellent support for scRNA-seq. M.P. is supported by the Sobek Foundation, the Ernst-Jung Foundation, the German Research Foundation (SFB 992, SFB1160, Reinhart-Koselleck-Grant, Gottfried Wilhelm Leibniz Prize) and the Ministry of Science, Research and Arts, Baden-Wuerttemberg (Sonderlinie "Neuroinflammation"). His research is supported by the German Research Foundation (DFG) under Germany's Excellence Strategy (CIBSS—EXC-2189—Project ID 390939984). J.P. received additional funding from the Berlin Institute of Health (CRG2aSP6), DFG (SFB/TRR265), and the UK DRI (Momentum Award). CL, MP, JP, CB and IH are supported by the SFB/TRR167. Open Access funding enabled and organized by ProjektDEAL.

Author contributions

Experiments and data analysis: PW, NH, RS, AS, LA, JK, AH, PZ, SB, TM; CNV-related turnover analysis: MG; Scientific input: TG, IH, FMVR; Embryonic pulse labeling experiments: NH, TM; Bulk RNA-Seq data analysis: OS; BM chimera data: CB, JP; scRNA-seq data analysis: RS; Project supervision and manuscript writing: PW, CL, MP.

Conflict of interest

The authors declare that they have no conflict of interest.

References

Ajami B, Bennett JL, Krieger C, Tetzlaff W, Rossi FMV (2007) Local self-renewal can sustain CNS microglia maintenance and function throughout adult life. *Nat Neurosci* 10: 1538 – 1543

Ajami B, Bennett JL, Krieger C, McNagny KM, Rossi FMV (2011) Infiltrating monocytes trigger EAE progression, but do not contribute to the resident microglia pool. *Nat Neurosci* 14: 1142 – 1149

Ajami B, Samusik N, Wieghofer P, Ho PP, Crotti A, Bjornson Z, Prinz M, Fantl WJ, Nolan GP, Steinman L (2018) Single-cell mass cytometry reveals distinct populations of brain myeloid cells in mouse neuroinflammation and neurodegeneration models. *Nat Neurosci* 21: 541 – 551

Anders S, Huber W (2010) Differential expression analysis for sequence count data. *Genome Biol* 11: R106

Andrews S (2010) FastQC: a quality control tool for high throughput sequence data. Available online at: http://www.bioinformatics.babraham.ac.uk/projects/fastqc

Baker SC, Bauer SR, Beyer RP, Brenton JD, Bromley B, Burrill J, Causton H, Conley MP, Elespuru R, Fero M *et al* (2005) The External RNA Controls Consortium: a progress report. *Nat. Methods* 2: 731 – 734

Bechmann I (2005) Failed central nervous system regeneration: a downside of immune privilege? *Neuromolecular Med* 7: 217 – 228

Benz C, Martins VC, Radtke F, Bleul CC (2008) The stream of precursors that colonizes the thymus proceeds selectively through the early T lineage precursor stage of T cell development. *J Exp Med* 205: 1187 – 1199

Boeck M, Thien A, Wolf J, Hagemeyer N, Laich Y, Yusuf D, Backofen R, Zhang P, Boneva S, Stahl A *et al* (2020) Temporospatial distribution and transcriptional profile of retinal microglia in the oxygen-induced retinopathy mouse model. *Glia* 68: 1859 – 1873

Boettcher C, Ulbricht E, Helmlinger D, Mack AF, Reichenbach A, Wiedemann P, Wagner H-J, Seeliger MW, Bringmann A, Priller J (2008) Long-term engraftment of systemically transplanted, gene-modified bone marrow-derived cells in the adult mouse retina. *Br J Ophthalmol* 92: 272 – 275

Boneva S, Schlecht A, Böhringer D, Mittelviefhaus H, Reinhard T, Agostini H, Auw-Haedrich C, Schlunck G, Wolf J, Lange C (2020) 3' MACE RNA-sequencing allows for transcriptome profiling in human tissue samples after long-term storage. *Lab Invest* 100: 1345 – 1355

Boyer SW, Schroeder AV, Smith-Berdan S, Forsberg EC (2011) All hematopoietic cells develop from hematopoietic stem cells through Flk2/Flt3-positive progenitor cells. *Cell Stem Cell* 9: 64 – 73

Butovsky O, Jedrychowski MP, Moore CS, Cialic R, Lanser AJ, Gabriely G, Koeglsperger T, Dake B, Wu PM, Doykan CE *et al* (2014) Identification of a unique TGF-β-dependent molecular and functional signature in microglia. *Nat Neurosci* 17: 131 – 143

Chappell-Maor L, Kolesnikov M, Kim J-S, Shemer A, Haimon Z, Grozovski J, Boura-Halfon S, Masuda T, Prinz M, Jung S (2020) Comparative analysis of CreER transgenic mice for the study of brain macrophages: a case study. *Eur J Immunol* 50: 353 – 362

Chinnery HR, Humphries T, Clare A, Dixon AE, Howes K, Moran CB, Scott D, Zakrzewski M, Pearlman E, McMenamin PG (2008) Turnover of bone marrow-derived cells in the irradiated mouse cornea. *Immunology* 125: 541 – 548

Dando SJ, Naranjo Golborne C, Chinnery HR, Ruitenberg MJ, McMenamin PG (2016) A case of mistaken identity: CD11c-eYFP(+) cells in the normal mouse brain parenchyma and neural retina display the phenotype of microglia, not dendritic cells. *Glia* 64: 1331 – 1349

Dobin A, Davis CA, Schlesinger F, Drenkow J, Zaleski C, Jha S, Batut P, Chaisson M, Gingeras TR (2013) STAR: ultrafast universal RNA-seq aligner. *Bioinformatics* 29: 15 – 21

Ensan S, Li A, Besla R, Degousee N, Cosme J, Roufaiel M, Shikatani EA, El-Maklizi M, Williams JW, Robins L *et al* (2016) Self-renewing resident arterial macrophages arise from embryonic CX3CR1(+) precursors and circulating monocytes immediately after birth. *Nat Immunol* 17: 159 – 168

Gautier EL, Shay T, Miller J, Greter M, Jakubzick C, Ivanov S, Helft J, Chow A, Elpek KG, Gordonov S *et al* (2012) Gene-expression profiles and transcriptional regulatory pathways that underlie the identity and diversity of mouse tissue macrophages. *Nat Immunol* 13: 1118 – 1128

Ginhoux F, Greter M, Leboeuf M, Nandi S, See P, Gokhan S, Mehler MF, Conway SJ, Ng LG, Stanley ER *et al* (2010) Fate mapping analysis reveals that adult microglia derive from primitive macrophages. *Science* 330: 841 – 845

Gloor BP (1969) Phagocytotic activity of the pigment epithelium after photocaogulation. (On the question of the origin of macrophages in the retina). *Albrecht Von Graefes Arch Klin Exp Ophthalmol* 179: 105 – 117

Goldmann T, Wieghofer P, Muller PF, Wolf Y, Varol D, Yona S, Brendecke SM, Kierdorf K, Staszewski O, Datta M *et al* (2013) A new type of microglia gene targeting shows TAK1 to be pivotal in CNS autoimmune inflammation. *Nat Neurosci* 16: 1618 – 1626

Goldmann T, Wieghofer P, Jordão MJC, Prutek F, Hagemeyer N, Frenzel K, Amann L, Staszewski O, Kierdorf K, Krueger M *et al* (2016) Origin, fate and dynamics of macrophages at central nervous system interfaces. *Nat Immunol* 17: 797 – 805

Grün D, Kester L, van Oudenaarden A (2014) Validation of noise models for single-cell transcriptomics. *Nat. Methods* 11: 637 – 640

Grün D, Muraro MJ, Boisset JC, Wiebrands K, Lyubimova A, Dharmadhikari G, van den Born M, van Es J, Jansen E, Clevers H *et al* (2016) *De novo*

prediction of stem cell identity using single-cell transcriptome data. *Cell Stem Cell* 19: 266 – 277

Hagemeyer N, Kierdorf K, Frenzel K, Xue J, Ringelhan M, Abdullah Z, Godin I, Wieghofer P, Costa Jordão MJ, Ulas T *et al* (2016) Transcriptome-based profiling of yolk sac-derived macrophages reveals a role for Irf8 in macrophage maturation. *EMBO J* 35: 1730 – 1744

Hamrah P, Huq SO, Liu Y, Zhang Q, Dana MR (2003) Corneal immunity is mediated by heterogeneous population of antigen-presenting cells. *J Leukoc Biol* 74: 172 – 178

Hashimshony T, Senderovich N, Avital G, Klochendler A, de Leeuw Y, Anavy L, Gennert D, Li S, Livak KJ, Rozenblatt-Rosen O *et al* (2016) CEL-Seq2: sensitive highly-multiplexed single-cell RNA-Seq. *Genome Biol* 17: 77

Herman JS, Sagar, Grün D (2018) FateID infers cell fate bias in multipotent progenitors from single-cell RNA-seq data. *Nat Methods* 15: 379 – 386

Huang Y, Xu Z, Xiong S, Qin G, Sun F, Yang J, Yuan T-F, Zhao L, Wang K, Liang Y-X *et al* (2018) Dual extra-retinal origins of microglia in the model of retinal microglia repopulation. *Cell Discov* 4: 9

Hume DA, Perry VH, Gordon S (1983) Immunohistochemical localization of a macrophage-specific antigen in developing mouse retina: phagocytosis of dying neurons and differentiation of microglial cells to form a regular array in the plexiform layers. *J Cell Biol* 97: 253 – 257

Jordão MJC, Sankowski R, Brendecke SM, Sagar LG, Tai Y-H, Tay TL, Schramm E, Armbruster S, Hagemeyer N *et al* (2019) Single-cell profiling identifies myeloid cell subsets with distinct fates during neuroinflammation. *Science* 363: eaat7554

Jung S, Aliberti J, Graemmel P, Sunshine MJ, Kreutzberg GW, Sher A, Littman DR (2000) Analysis of fractalkine receptor CX(3)CR1 function by targeted deletion and green fluorescent protein reporter gene insertion. *Mol Cell Biol* 20: 4106 – 4114

Kaur C, Foulds WS, Ling EA (2008) Blood-retinal barrier in hypoxic ischaemic conditions: basic concepts, clinical features and management. *Prog Retin Eye Res* 27: 622 – 647

Kezic J, Xu H, Chinnery HR, Murphy CC, McMenamin PG (2008) Retinal microglia and uveal tract dendritic cells and macrophages are not CX3CR1 dependent in their recruitment and distribution in the young mouse eye. *Invest Ophthalmol Vis Sci* 49: 1599 – 1608

Kierdorf K, Erny D, Goldmann T, Sander V, Schulz C, Perdiguero EG, Wieghofer P, Heinrich A, Riemke P, Hölscher C *et al* (2013a) Microglia emerge from erythromyeloid precursors via Pu.1- and Irf8-dependent pathways. *Nat Neurosci* 16: 273 – 280

Kierdorf K, Katzmarski N, Haas CA, Prinz M (2013b) Bone marrow cell recruitment to the brain in the absence of irradiation or parabiosis bias. *PLoS One* 8: e58544

Kierdorf K, Masuda T, Jordão MJC, Prinz M (2019) Macrophages at CNS interfaces: ontogeny and function in health and disease. *Nat Rev Neurosci* 9: 547 – 562

van de Laar L, Saelens W, De Prijck S, Martens L, Scott CL, Van Isterdael G, Hoffmann E, Beyaert R, Saeys Y, Lambrecht BN *et al* (2016) Yolk Sac macrophages, fetal liver, and adult monocytes can colonize an empty niche and develop into functional tissue-resident macrophages. *Immunity* 44: 755 – 768

Law CW, Chen Y, Shi W, Smyth GK (2014) voom: Precision weights unlock linear model analysis tools for RNA-seq read counts. *Genome Biol* 15: R29

Li H, Durbin R (2010) Fast and accurate long-read alignment with Burrows-Wheeler transform. *Bioinformatics* 26: 589 – 595

Liao Y, Smyth GK, Shi W (2014) featureCounts: an efficient general purpose program for assigning sequence reads to genomic features. *Bioinformatics* 30: 923 – 930

Liu J, Xue Y, Dong D, Xiao C, Lin C, Wang H, Song F, Fu T, Wang Z, Chen J *et al* (2017) CCR2- and CCR2+ corneal macrophages exhibit distinct characteristics and balance inflammatory responses after epithelial abrasion. *Mucosal Immunol* 10: 1145 – 1159

Ma W, Zhang Y, Gao C, Fariss RN, Tam J, Wong WT (2017) Monocyte infiltration and proliferation reestablish myeloid cell homeostasis in the mouse retina following retinal pigment epithelial cell injury. *Sci Rep* 7: 8433

Ma W, Silverman SM, Zhao L, Villasmil R, Campos MM, Amaral J, Wong WT (2019) Absence of TGFβ signaling in retinal microglia induces retinal degeneration and exacerbates choroidal neovascularization. *Elife* 8: e42049

Masuda T, Sankowski R, Staszewski O, Böttcher C, Amann L, Sagar, Scheiwe C, Nessler S, Kunz P, van Loo G*et al* (2019) Spatial and temporal heterogeneity of mouse and human microglia at single-cell resolution. *Nature* 566: 388 – 392

Masuda T, Amann L, Sankowski R, Staszewski O, Lenz M, D Errico P, Snaidero N, Costa Jordão MJ, Böttcher C, Kierdorf K *et al* (2020) Novel Hexb-based tools for studying microglia in the CNS. *Nat Immunol* 21: 802 – 815

Mildner A, Schmidt H, Nitsche M, Merkler D, Hanisch U-K, Mack M, Heikenwalder M, Brück W, Priller J, Prinz M (2007) Microglia in the adult brain arise from Ly-6ChiCCR2+ monocytes only under defined host conditions. *Nat Neurosci* 10: 1544 – 1553

Molawi K, Wolf Y, Kandalla PK, Favret J, Hagemeyer N, Frenzel K, Pinto AR, Klapproth K, Henri S, Malissen B *et al* (2014) Progressive replacement of embryo-derived cardiac macrophages with age. *J Exp Med* 211: 2151 – 2158

Mudge JM, Harrow J (2015) Creating reference gene annotation for the mouse C57BL6/J genome assembly. *Mamm Genome* 26: 366 – 378

O'Koren EG, Yu C, Klingeborn M, Wong AYW, Prigge CL, Mathew R, Kalnitsky J, Msallam RA, Silvin A, Kay JN *et al* (2019) Microglial function is distinct in different anatomical locations during retinal homeostasis and degeneration. *Immunity* 50: 723 – 737.e7

Oh H, Takagi H, Takagi C, Suzuma K, Otani A, Ishida K, Matsumura M, Ogura Y, Honda Y (1999) The potential angiogenic role of macrophages in the formation of choroidal neovascular membranes. *Invest Ophthalmol Vis Sci* 40: 1891 – 1898

Perdiguero EG, Klapproth K, Schulz C, Busch K, Azzoni E, Crozet L, Garner H, Trouillet C, de Bruijn MF, Geissmann F *et al* (2014) Tissue-resident macrophages originate from yolk-sac-derived erythro-myeloid progenitors. *Nature* 518: 547 – 551

Pitulescu ME, Schmidt I, Benedito R, Adams RH (2010) Inducible gene targeting in the neonatal vasculature and analysis of retinal angiogenesis in mice. *Nat Protoc* 5: 1518 – 1534

Prinz M, Jung S, Priller J (2019) Microglia biology: one century of evolving concepts. *Cell* 179: 292 – 311

Saederup N, Cardona AE, Croft K, Mizutani M, Cotleur AC, Tsou C-L, Ransohoff RM, Charo IF (2010) Selective chemokine receptor usage by central nervous system myeloid cells in CCR2-red fluorescent protein knock-in mice. *PLoS One* 5: e13693

Sankowski R, Böttcher C, Masuda T, Geirsdottir L, Sagar, Sindram E, Seredenina T, Muhs A, Scheiwe C, Shah MJ *et al* (2019) Mapping microglia states in the human brain through the integration of high-dimensional techniques. *Nat Neurosci* 22: 2098 – 2110

Santos AM, Calvente R, Tassi M, Carrasco M-C, Martín-Oliva D, Marín-Teva JL, Navascués J, Cuadros MA (2008) Embryonic and postnatal development of microglial cells in the mouse retina. *J Comp Neurol* 506: 224 – 239

Schlecht A, Boneva S, Gruber M, Zhang P, Horres R, Bucher F, Auw-Haedrich C, Hansen L, Stahl A, Hilgendorf I *et al* (2020) Transcriptomic characterization of human choroidal neovascular membranes identifies calprotectin as a novel biomarker for patients with age-related macular degeneration. *Am J Path* 190: 1632 – 1642

Schulz C, Gomez Perdiguero E, Chorro L, Szabo-Rogers H, Cagnard N, Kierdorf K, Prinz M, Wu B, Jacobsen SEW, Pollard JW *et al* (2012) A lineage of myeloid cells independent of Myb and hematopoietic stem cells. *Science* 336: 86 – 90

Shechter R, London A, Schwartz M (2013) Orchestrated leukocyte recruitment to immune-privileged sites: absolute barriers versus educational gates. *Nat Rev Immunol* 13: 206 – 218

Streilein JW (2003) Ocular immune privilege: therapeutic opportunities from an experiment of nature. *Nat Rev Immunol* 3: 879 – 889

Tay TL, Mai D, Dautzenberg J, Fernández-Klett F, Lin G, Sagar, Datta M, Drougard A, Stempfl T, Ardura-Fabregat A *et al* (2017) A new fate mapping system reveals context-dependent random or clonal expansion of microglia. *Nat Neurosci* 20: 793 – 803

Tobe T, Ortega S, Luna JD, Ozaki H, Okamoto N, Derevjanik NL, Vinores SA, Basilico C, Campochiaro PA (1998) Targeted disruption of the FGF2 gene does not prevent choroidal neovascularization in a murine model. *Am. J. Pathol.* 153: 1641 – 1646

Trapnell C, Cacchiarelli D, Grimsby J, Pokharel P, Li S, Morse M, Lennon NJ, Livak KJ, Mikkelsen TS, Rinn JL (2014) Pseudo-temporal ordering of individual cells reveals dynamics and regulators of cell fate decisions. *Nat Biotechnol* 32: 381 – 386

Varol C, Mildner A, Jung S (2015) Macrophages: development and tissue specialization. *Annu Rev Immunol* 33: 643 – 675

Wang L, Feng Z, Wang X, Wang X, Zhang X (2010) DEGseq: an R package for identifying differentially expressed genes from RNA-seq data. *Bioinformatics* 26: 136 – 138

Wang X, Zhao L, Zhang J, Fariss RN, Ma W, Kretschmer F, Wang M, Qian HH, Badea TC, Diamond JS *et al* (2016) Requirement for microglia for the maintenance of synaptic function and integrity in the mature retina. *J Neurosci* 36: 2827 – 2842

Warnes GR, Bolker B, Bonebakker L, Gentleman R, Huber W, Liaw A, Lumley T, Maechler M, Magnusson A, Moeller S *et al* (2016) Various R Programming Tools for Plotting Data. R package version 3.0.1. Available online at: https://CRAN.R-project.org/package=gplots

Wieghofer P, Knobeloch K-P, Prinz M (2015) Genetic targeting of microglia. *Glia* 63: 1 – 22

Wieghofer P, Prinz M (2015) Genetic manipulation of microglia during brain development and disease. *Biochim Biophys Acta* 1862: 299 – 309

Winget S (2011) FastQ Screen allows you to screen a library of sequences in FastQ format against a set of sequence databases so you can see if the composition of the library matches with what you expect. Available online at: https://www.bioinformatics.babraham.ac.uk/projects/fastq_screen/

Xu H, Chen M, Mayer EJ, Forrester JV, Dick AD (2007) Turnover of resident retinal microglia in the normal adult mouse. *Glia* 55: 1189 – 1198

Yona S, Kim K-W, Wolf Y, Mildner A, Varol D, Breker M, Strauss-Ayali D, Viukov S, Guilliams M, Misharin A *et al* (2013) Fate mapping reveals origins and dynamics of monocytes and tissue macrophages under homeostasis. *Immunity* 38: 79 – 91

Zajac BK, Amendt J, Horres R, Verhoff MA, Zehner R (2015) De novo transcriptome analysis and highly sensitive digital gene expression profiling of Calliphora vicina (Diptera: Calliphoridae) pupae using MACE (Massive Analysis of cDNA Ends). *Forensic Sci Int Genet* 15: 137 – 146